STUDIES OF NEUTRON-ARGON INTERACTIONS IN MINI-CAPTAIN

A Dissertation Presented to

the Faculty of the Department of Physics

University of Houston

In Partial Fulfillment

of the Requirements for the Degree

Doctor of Philosophy

By

Babu Ram Bhandari

December 2016

STUDIES OF NEUTRON-ARGON INTERACTIONS IN MINI-CAPTAIN

Babu Ram Bhandari

APPROVED:

Dr. Lisa Whitehead
Department of Physics

Dr. Rene Bellwied
Department of Physics

Dr. Kwong Lau
Department of Physics

Dr. Eric R. Bittner
Department of Chemistry

Dean, College of Natural Sciences and Mathematics

This thesis would not have been possible without Dr. Lisa Whitehead. I am extremely grateful to you for your guidance and support throughout my graduate school. Your advice and assistance has been invaluable.

I would like to thank all CAPTAIN collaborators. Big thank goes to Dr. Clark McGrew, Dr. Elena Guardincerri and Peter Madigan. I would also like to thank my group members, Dr. Aaron Pichardo, Jieun yoo, Ian Mitchell and Dani Morris for their continuous support and encouragement.

I am truly indebted and thankful to my families for the sacrifices they made while helping me achieve what I have, their constant support is something I could not have done without.

This work is supported by Department of Energy, Office of Science. I would like to thank the Department of Energy for supporting our research.

STUDIES OF NEUTRON-ARGON INTERACTIONS IN MINI-CAPTAIN

An Abstract of a Dissertation

Presented to

the Faculty of the Department of Physics

University of Houston

In Partial Fulfillment

of the Requirements for the Degree

Doctor of Philosophy

By

Babu Ram Bhandari

December 2016

Abstract

The Deep Underground Neutrino Experiment (DUNE) will use a large underground liquid argon time projection chamber (LArTPC) to study neutrino oscillations, search for proton decay, and observe supernova neutrinos, should a supernova occur. There is a currently a rich program of R&D on LArTPCs in preparation for DUNE. The Cryogenic Apparatus for Precision Tests of Argon Interactions with Neutrino (CAPTAIN) program is one of these R&D efforts. This thesis describes studies on the neutron interactions in liquid argon using the mini-CAPTAIN LArTPC at a neutron beam facility at Los Alamos National Laboratory. Studies of neutron signatures can help to improve neutrino energy reconstruction in DUNE, important for the neutrino oscillation measurements. In addition, neutron data can be used to measure cross sections of the neutron background to supernova burst neutrinos. This work represents the first measurement of neutron interactions in a liquid argon TPC in the energy range above 20 MeV.

Contents

List of Figures

List of Tables

Chapter 1

Introduction

Neutrinos are unique subatomic particles. The fact that they display extraordinary properties that are unmatched by any other particles makes the field of neutrino physics full of both challenges and opportunities. For instance, due to their extremely low interaction rate, neutrinos have the ability to travel several light years through a solid material without interacting. On the one hand, this property makes them elusive and difficult to study. On the other hand, it is precisely the fact that they interact so differently from other particles that has led the way to the formulation of ground-breaking physics theories and a deeper understanding of our universe.

Neutrinos are electrically neutral particles of spin $\frac{1}{2}$ with a very tiny mass, at least a million times less than the mass of an electron. There are three flavors of neutrinos, ν_e, ν_μ, and ν_τ , are left-handed, and their antiparticles, $\bar{\nu_e}$, $\bar{\nu_\mu}$, and $\bar{\nu_\tau}$, are right-handed. After the photon, the neutrino is the most abundant particle in the Universe. It also arrives unscathed from the farthest reaches of the Universe, carrying information about its source. The interactions of neutrinos are mediated by heavy $W^{\pm}$ and Z^0 bosons. Neutrino detection requires a very large detector and/or very intense neutrino beams.

1.1 Neutrino Oscillations

Neutrino oscillations arise from the situation that mass and flavor states do not coincide. Both flavor and mass states form orthonormal bases in Hilbert space. One can change between bases with help of a matrix, U, a rotation matrix which maps the flavor basis onto the mass basis [2]. In the most general case, U can be complex and, as a rotation matrix, must be unitary. In this picture, a neutrino flavor state can be written as a superposition of the mass states

$$|\nu_\alpha\rangle = \sum_{i=1}^{N} U^*_{\alpha i}|\nu_i\rangle \tag{1.1}$$

Where $U^*_{\alpha i}$ are the elements of the matrix U^*. It is called the complex conjugate of the neutrino mixing matrix or Pontecorvo Maki Nakagawa Sakata (PMNS) matrix [3].

In the instant of a neutrinos creation, it is encountered in a pure flavor state, as described by Equation 1.1. In radioactive β-decay, for example, the neutrino is initially in a pure electron neutrino flavor state. The oscillaiton phenomenon occurs when the neutrino travels through space and time. In natural units, the time evolution of the initial flavor state is given by

$$|\nu_i(t)\rangle = e^{-iE_i t}|\nu_i\rangle \tag{1.2}$$

where t is the time elapsed since the creation and

$$E_i = \sqrt{p^2 + m_i^2} \tag{1.3}$$

is the relativistic energy of the mass state $|\nu_i\rangle$. If all neutrino masses were exactly equal, E_i would also be equal for all mass eigenstates and they would evolve identically according to Equation 1.2. There would be no oscillations in the scenario. In the case of different neutrino masses, however, equations 1.2 and 1.3 do lead to different evolutions of the states. In consequence, the originally pure flavor state from equation 1.1 changes its position with time and gains contributions from the other flavor states as well. At the moment of its detection the evolved flavor state $|\nu_\alpha(t)\rangle$ is collapsed onto a final flavor eigenstate $\langle\nu_\beta|$. Since the final state can also be described by a superposition of mass eigenstates, the projection yields

$$\langle\nu_\beta|\nu_\alpha(t)\rangle = \sum_j \langle\nu_j|U^+_{j\beta} \cdot \sum_i e^{-iE_it} U_{\alpha i}|\nu_i\rangle = \sum_n e^{-iE_nt} U^+_{n\beta} U_{\alpha n} \tag{1.4}$$

where U^+ is the conjugate transpose of U. For the second equality, the orthonormality of the states $\langle\nu_\alpha|\nu_\beta\rangle = \delta_{\alpha\beta}$ was used.

Equation 1.4 gives the quantum-mechanical amplitude to encounter the neutrino, which was created with flavor, α and energy E, with the flavor β after a time t. The probability $P_{\alpha\rightarrow\beta}$ to detect the neutrino with flavor β is the square of the absolute value of the amplitude:

$$
\begin{aligned}
P(\nu_\alpha \to \nu_\beta)(t) &= |\langle \nu_\beta | \nu_\alpha(t) \rangle|^2 \\
&= \delta_{\alpha\beta} - 4 \sum_{i>j} Re(U^*_{\alpha i} U_{\beta i} U_{\alpha j} U^*_{\beta j}) \sin^2(\frac{\Delta m^2_{ij} L}{4E}) \\
&+ 2 \sum_{i>j} Im(U^*_{\alpha i} U_{\beta i} U_{\alpha j} U^*_{\beta j}) \sin^2(\frac{\Delta m^2_{ij} L}{2E})
\end{aligned}
\tag{1.5}
$$

where $\delta_{\alpha\beta}$ is Kronecker delta, $\Delta m^2_{ij} = m^2_i - m^2_j$, L is length, and E is energy of neutrino.

	parameter	Value
Mass difference	Δm^2_{21}	$(7.50^{+0.19}_{-0.20}).10^{-5}\ eV^2$
	Δm^2_{32}	$(2.32^{+0.12}_{-0.08}).10^{-3}\ eV^2$
	Δm^2_{31}	$\approx \Delta m^2_{32}$
Mixing angles	$Sin^2(2\theta_{12})$	$0.857^{+0.023}_{-0.025}$
	$Sin^2(2\theta_{23})$	> 0.95 (95% CL)
	$Sin^2(2\theta_{13})$	0.095 ± 0.010

Table 1.1: Neutrino oscillation parameters. The values cited here are taken from [3]. In the case of Δm^2_{31} and Δm^2_{32} the sign is still unknown and only the absolute value is given

1.1.1 PMNS-matrix and mixing angles

The mixing matrix U can be written as for four flavor neutrinos is:

$$U = \begin{pmatrix} 1 & 0 & 0 \\ 0 & c_{23} & s_{23} \\ 0 & -s_{23} & c_{23} \end{pmatrix} \begin{pmatrix} c_{13} & 0 & s_{13}e^{-i\delta} \\ 0 & 1 & 0 \\ -s_{13}e^{i\delta} & 0 & c_{13} \end{pmatrix} \begin{pmatrix} c_{12} & s_{12} & 0 \\ -s_{12} & c_{12} & 0 \\ 0 & 0 & 1 \end{pmatrix} \begin{pmatrix} e^{i\alpha_1/2} & 0 & 0 \\ 0 & e^{i\alpha_2/2} & 0 \\ 0 & 0 & 1 \end{pmatrix} \tag{1.6}$$

where $c_{ij} = cos\theta_{ij}$ and $s_{ij} = sin\theta_{ij}$. The θ_{ij} are a measure of the oscillation amplitude and are called neutrino mixing angles in analogy to the mixing angles in the quark sector. The parametrization also contains a complex phase δ for the possibility of CP violation, as well as two phases α_1 and α_2 for the case that neutrinos should turn out to be Majorana particles. With this matrix, U, the probability of electron neutrino becomes

$$P_{\nu_e \to \nu_e} = 1 - 4cos^2\theta_{12}cos^4\theta_{13}sin^2\theta_{12}sin^2\left(\frac{\Delta m^2_{12}}{4E}L\right) - 4cos^2\theta_{12}cos^2\theta_{13}sin^2\theta_{13}sin^2\left(\frac{\Delta m^2_{13}}{4E}L\right) - 4sin^2\theta_{12}cos^2\theta_{13}sin^2\theta_{13}sin^2\left(\frac{\Delta m^2_{23}}{4E}L\right) \tag{1.7}$$

As of the time of this writing, only the complex phases α_1,α_2, and δ are unknown. All mixing angles have been determined experimentally, the latest being θ_{13}.

The values for the mixing angles and the squared mass differences are summarized in Table 1.1. Based upon these values, the survival and oscillation probability of an electron anti-neutrino in the three-neutrino case is illustrated in Figure 1.1.

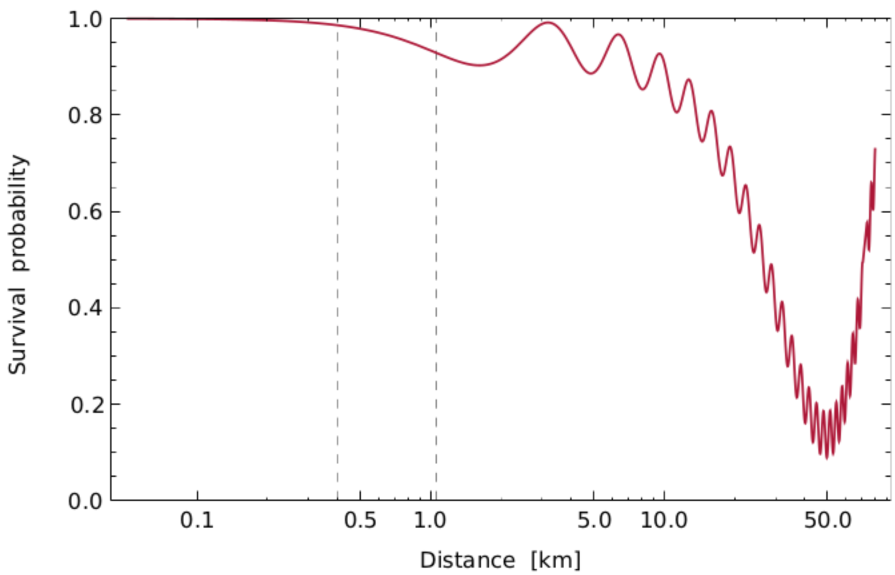

Figure 1.1: Survival probability of an electron antineutrino of 3 MeV kinetic energy in dependence on the distance traveled. The oscillation parameters are taken from Table 1.1 and this plot is taken from [3]

1.2 Open Questions

Their extremely small masses and the weak interaction probability of neutrinos frequently pose challenges for the measurement of neutrino properties. Their mere existence took about 26 years to be proven experimentally [4] and many questions concerning them are still unresolved today.

1.2.1 Dirac and Majorana nature

The discovery of neutrino oscillations showed that neutrinos have mass. Their lack of electrical charge and their non-zero mass opens up the possibility that neutrinos are Majorana fermions instead of Dirac fermions, i.e. that they are their own antiparticles.

A promising experimental way to search for the Majorana nature of neutrinos is neutrinoless double beta decay. In the ordinary double beta decay, an isotope simultaneously emits two electrons and two electron antineutrinos. This decay can be observed when a single beta decay would lead to a daughter nucleus with higher binding energy and is energetically forbidden. This is the case when ^{76}Ge decays via double beta decay into ^{76}Se. There are four particles involved in the decay, the two electrons exhibit a continuous energy spectrum.

Neutrinoless double beta decay is only possible if the neutrino is indeed a Majorana particle. The process can be imagined as an annihilation of the two neutrinos and only the two electrons are emitted. This process would violate total lepton number conservation by two numbers. As there are no neutrinos emitted, the two electrons receive the total decay energy. Experiments like **GERDA** look for a peak at the end of the double beta energy spectrum. In a first analysis by the GERDA collaboration, no peak was found [3]. The sensitivity of the experiment will be increased by a factor of 10 in its second phase.

1.2.2 Neutrino Mass

From the day of their postulation, it was clear that neutrinos can only have a very tiny mass (otherwise it would have been visible in the endpoint of the β spectrum), For a long time it was widely believed that neutrinos were in fact massless. The discovery of neutrino oscillations showed that neutrinos have non-zero mass [2] and allowed a measurement of the squared mass differences, but the absolute mass remains unknown. The current best limit on the effective neutrino mass

$$m_{\bar{\nu}_e}^{eff} = \sqrt{\sum_i |U_{ei}|^2 m_{\nu_i}^2} \tag{1.8}$$

was determined in the Mainz and Troitsk experiments via the end point of the tritium β^- spectrum. They found an upper limit of 2.3 eV (95 % CL) [5] and 2.2 eV (95 % CL) [6], respectively. The **KATRIN** experiment improves on this method and has a projected sensitivity of 0.2 eV [7].

All of these experiments work with electron antineutrinos. As the effective mass involves the PMNS-matrix, U, it could be different for electron neutrinos if there is CP-violation in the lepton sector. The best experimental limit on $m_{\nu_e}^{eff}$ comes from a measurement with electron capture on ^{163}Ho (which involves a neutrino, rather than an antineutrino) and is 225 eV [8]. The upcoming experiments, MARE and ECHO, intend to improve this limit and make use of Rhenium and Holmium, respectively [9].

1.2.3 Neutrino Mass Hierarchy

Closely related to the neutrino masses is the question of the neutrino mass hierarchy, i.e. the ordering of the mass eigenvalues as shown in Figure 1.2. This question is equivalent to determining the signs of the squared mass differences, Δm_{ij}^2, between the neutrino flavors, i and j. It is already known that Δm_{21}^2 is positive, i.e.$m_2 > m_1$. The signs of Δm_{31}^2 and Δm_{32}^2 are still unknown [3]. The mass hierarchy is of special interest, since the direct experimental discovery of all three absolute neutrino masses may still lie in the far future. Together with a known mass hierarchy, however, it is sufficient to measure the mass of a single neutrino eigenstate to know the absolute masses of the other two as well.

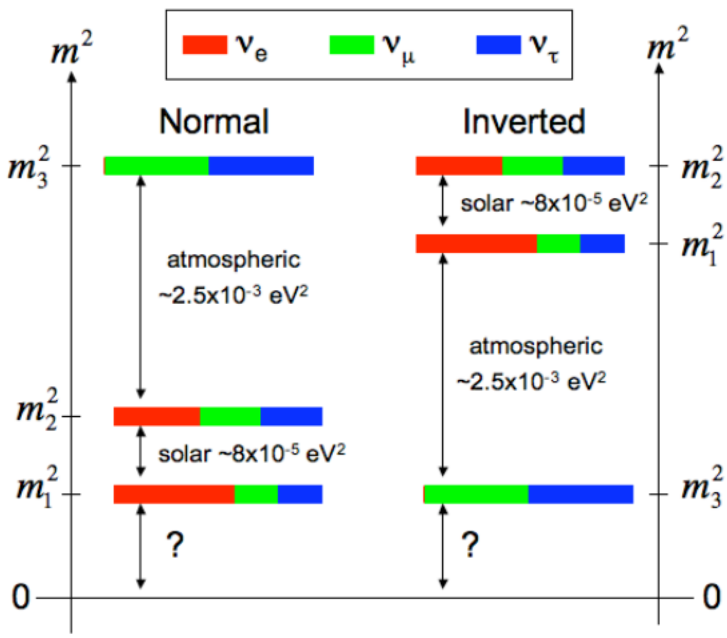

Figure 1.2: Mass hierarchy [4]

1.2.4 Sterile Neutrinos

Sterile neutrinos are hypothetical particles that interact only via gravity and do not interact via any of the other fundamental interactions of the Standard Model. The "sterility" is required to avoid a clash with the number of neutrino flavors predicted by the Z-Boson lifetime. Different observations constrain the number of weakly-interacting neutrinos (with a mass below half of the Z-Boson mass) to three, but a non-interacting neutrino could circumvent this restriction.

1.2.5 CP-Violation

CP-symmetry states that the laws of physics should be the same if a particle is interchanged with its antiparticle (C symmetry), and when its spatial coordinates are inverted ("mirror" or P symmetry). As already mentioned before, equation 1.5 represents the oscillation of neutrinos, not antineutrinos. In the case of antineutrinos the formula has to be conjugated and U is replaced by U^*. If the CP-violating phase δ in equation 1.6 is not equal to zero, U^* is different from $\mathbf{U}$. In consequence, CP-violations could manifest in a different oscillation behavior of neutrinos and antineutrinos [2].

1.3 Supernova Neutrinos

When a massive star has exhausted its nuclear fuel, it collapses to form a compact object such as a neutron star or a black hole. A prominent feature of the collapse is that 99% of the gravitational binding energy of the resulting remnant is converted to neutrinos with energies of a few tens of MeV over a timescale of a few tens of seconds. This highly efficient energy loss via neutrinos occurs because the neutrinos interact only via the weak interaction and can escape easily, whereas photons are trapped [10].

Neutrinos were observed for the celebrated 1987A core-collapse supernova (SN1987A) in the Large Magellanic Cloud (LMC), 50 kpc away from Earth. Two water Cherenkov detectors, Kamiokande-II [11] and the Irvine-Michigan- Brookhaven (IMB) experiment [12], observed 19 neutrino interaction events between them over a 13-s interval at a time consistent with the estimated time of the core collapse. Two scintillator detectors, Baksan [13] and LSD [14], also reported observations; the latter report was controversial because the events were recorded several hours early. Figure 1.4 shows energy vs time for neutrinos observed by Kamiokande, IMB, and Baksan. Although these events were a meager sample, the SN1987A neutrino events were sufficient to confirm the baseline model of core collapse. Beyond that, they have provided a very wide range of constraints on astrophysics and physics [15], resulting in the publication of hundreds of papers, which continues to this day.

Worldwide capabilities for supernova neutrino detection have increased by orders of magnitude since 1987. The next observation of a nearby core-collapse supernova will provide a great deal of information for both physics and astrophysics. The rate of core-collapse supernovae is estimated to be a few per century [16] in a galaxy such as the Milky Way, so the chance of observing one in the next few decades is not negligible. The most likely distance of the next core-collapse supernova from

Earth is between 12 and 15 kpc, according to the distribution of possible supernova progenitors in the Milky Way [17].

Despite enormous recent progress, much about the physics of core collapse is not well understood. The neutrino messengers from deep inside the supernova will help us understand many aspects of the supernova mechanism and associated phenomena. The neutrinos are probably intimately involved with the explosion mechanism; imprinted on the flux will be signatures of shock waves, accretion, cooling, possible formation of exotic matter, and further collapse to a black hole. An improved understanding of supernova nucleosynthesis will result from a detection. The expected supernova neutrino spectra (integrated over 10 s) for the different flavor components are shown in Figure 1.3.

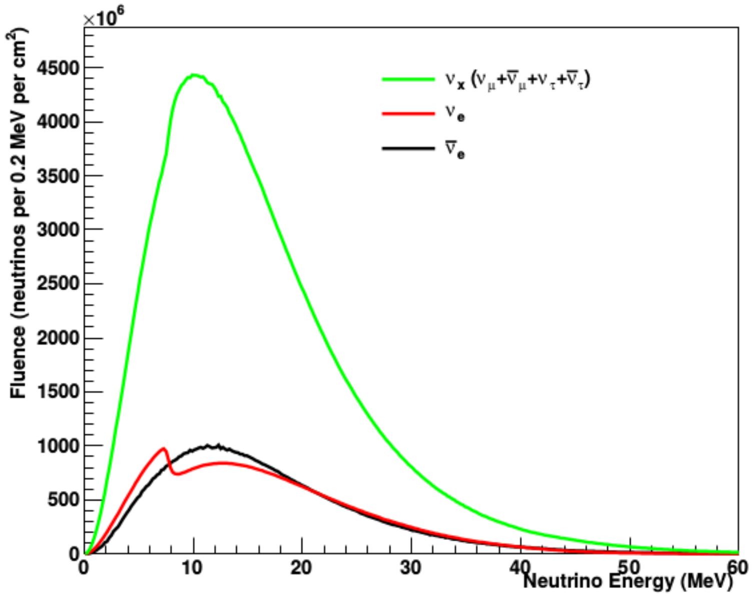

Figure 1.3: Example of the expected supernova neutrino spectra (integrated over 10 s) for the different flavor components [10].

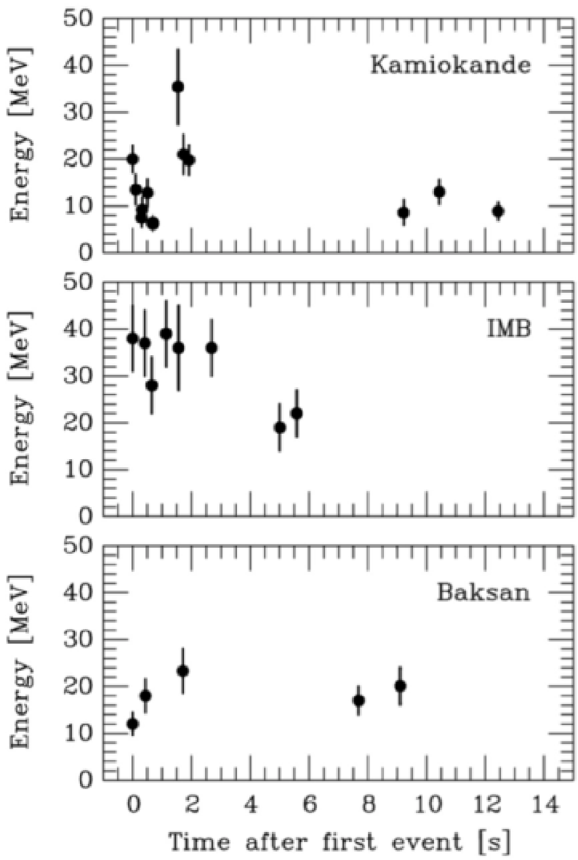

Figure 1.4: Supernova neutrino observation from different experiment at 50 kpc [18].

1.4 DUNE Experiment

Deep Underground Neutrino Experiment (DUNE) is a international, leading-edge, dual-site experiment for neutrino science and proton decay studies [4]. The Long Baseline Neutrino Facility (LBNF) is a facility for a high intensity neutrino beam. Together, LBNF and DUNE will comprise the worlds highest-intensity neutrino beam at Fermilab, in Batavia, IL, a high-precision near detector on the Fermilab site, a massive liquid argon time projection chamber (LArTPC) far detector installed deep underground at the Sanford Underground Research Facility (SURF) 1300 km away in Lead, SD, and all of the conventional and technical facilities necessary to support the beamline and detector system, Figure 1.5.

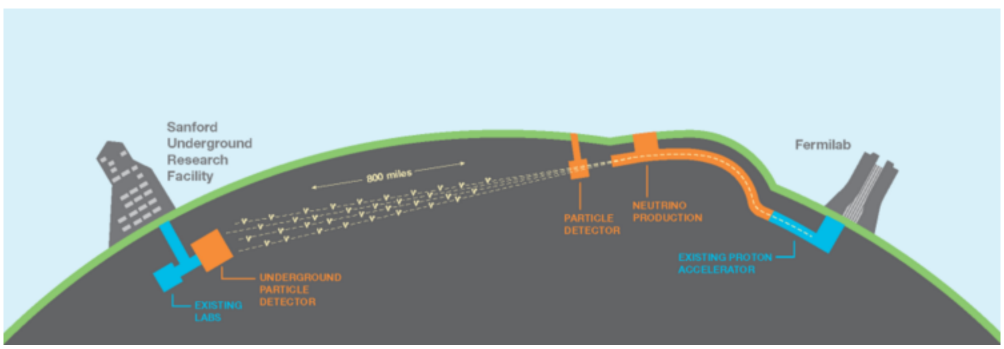

Figure 1.5: Schematic view of DUNE [4].

LBNF/DUNE will address fundamental questions key to our understanding of the Universe. These include

- What is the origin of the matter-antimatter asymmetry in the Universe?
- What are the the fundamental underlying symmetries of the Universe?
- Is there a Grand Unified Theory of the Universe?
- How do supernovae explode and what new physics will we learn from a neutrino burst?

1.4.1 Physics Goals of DUNE

The matter-anti matter asymmetry of the universe is one of the key scientific questions of our time. In order to explain the asymmetry, a large violation of CP symmetry (particle vs. antiparticle behavior) is required. Of the two types of matter particles - quarks and leptons - extensive studies of CP violation with quarks have been made and found to be too small to explain the asymmetry of matter and anti-matter in the universe. The discovery of neutrino oscillation gives us a mechanism to search for CP violation with leptons. Over the last 15 years, several experiments have contributed to the discovery of neutrino oscillations by measuring individual components of the leptonic mixing matrix.

DUNE will be able to determine the neutrino mass hierarchy and to have a chance to directly measure the leptonic CP violating phase δ by studying neutrino flavor oscillation over a very long baseline for a broad energy spectrum. As claimed by

DUNE experiment, the required physics sensitivity can be reached with a powerful neutrino beam coupled to a giant LArTPC, placed deep underground at a baseline of 1300 km. The fact that the LAr TPC detector digitally records the electronic image of ionizing events with mm-size resolution allows us to obtain unique tracking and calorimetric capabilities. Due to the large mass of the detector and the low background with a high sensitivity, the detector will also be able to set new limits on nucleon decay lifetimes and to detect neutrinos from astrophysical sources, such as core-collapse supernova and dark matter annihilations.

DUNE will measure CP violation by making detailed studies of oscillation phenomenon over a broad range of neutrino and antneutrino energies. While this comprehensive approach allows for the most precise measurements, it presents unique challenges that must be addressed. Oscillation phenomenon depend on the flavor and energy of the neutrino, the distance between the point of production and the point of measurement, and element of the leptonic mixing matrix. To measure the mixing matrix elements with neutrino oscillations, DUNE will measure the conversion probability of one neutrino flavor to another as a function of the true neutrino energy. CP violation induces a difference in the energy-dependent probability between conversion of neutrinos and conversion of antineutrinos. DUNE will run with a broad band neutrino beam and a broad-band antineutrino beam and therefore must reconstruct the neutrino energy on an event by event basis in the far detector using the information from particles generated by the (anti)neutrino reaction. At DUNE energies, the particles generated include charged leptons, mesons, protons, and neutrons. While most particles will be well measured in the far detector, a LArTPC, neutrons are the exception. Neutrons can carry away significant energy in neutrino interactions at neutrino energies relevant to DUNE. Furthermore, the fraction of energy they carry away differs between interactions involving neutrino interactions vs. antineutrino interactions as shown in Figure 1.6. To produce a reliable result with the highest possible sensitivity, it is paramount to account for the energy lost in neutrons when reconstructing the neutrino energy. In order to achieve this goal, we must understand the neutron interactions in a liquid argon TPC.

The Figure 1.6 shows the ratio of visible to true energy of muon neutrino and muon-antineutrino neglecting all the neutron energy. It clearly shows energy is missing in the reconstruction. We want to improve neutrino energy reconstruction by studying the signature of neutrons in liquid argon (LAr).

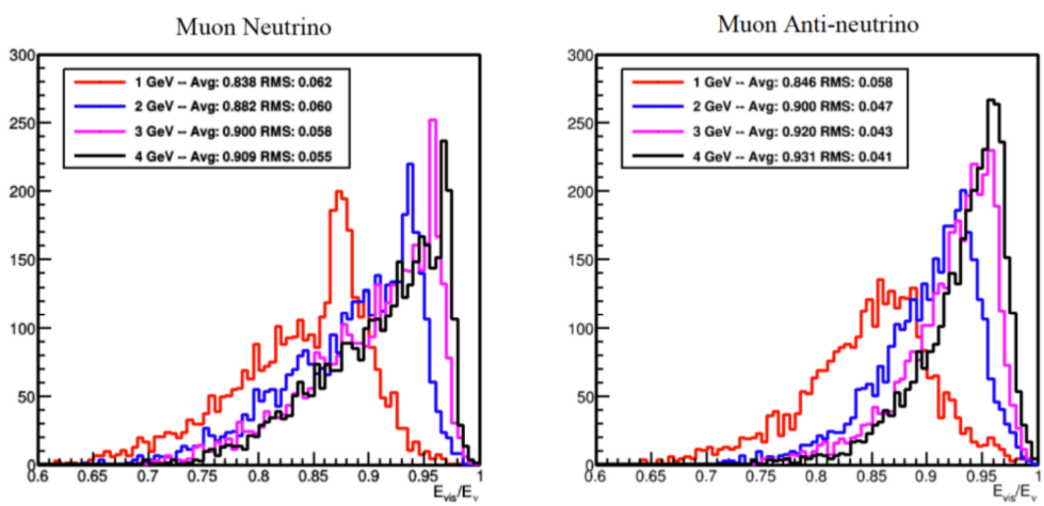

Figure 1.6: Ratio of visible to true energy for muon neutrinos and antineutrinos interacting in a LAr TPC as predicted by Monte Carlo simulations. These plots assume all the missing energy is from neutrons. Figure by Clark McGrew [19].

1.5 Thesis Organization

Chapter 2 describes the basic principle of the detector and is therefore the foundation to the detector response studies that are presented in later chapters. Due to the relevance for the thesis, we first describe the energy loss of heavy charged particles with moderate velocities. Then, the fundamental ionization and scintillation processes are discussed. In order to understand the response of the LAr-TPC, the charge transport including electron drifts in LAr are detailed. Finally, the signal induction on the 2D anode is explained.

In Chapter 3, we describe the mini-CAPTAIN experiment. We also explain the wire plane and cryostat system in detail in this chapter.

Chapter 4 discusses the photon detection system. This chapter talks about the how scintillation light produced in liquid argon and how it can be detected with the PMTs. Chapter 5 describes studies the neutron interactions in a liquid argon TPC.

Finally Chapter 6 and Chapter 7 describes the data analysis and conclusion.

Chapter 2

Liquid Argon Time Projection Chamber

2.1 Liquid Argon (LAr) Properties

The choice of liquid argon as detector medium has been motivated in the literature [20]. LAr allows the drifting of ionization electrons with a high drift speed (2 mm/μs at 1 kV/cm) and small diffusion ($<$ 1 mm for 1 m) over large distances up to several meters without significant degradation of the imaging quality. Since the scintillation in LAr is detectable and orders of magnitudes faster ($\tau_s \approx 6\ ns$ and $\tau_t \approx 1.6\ \mu s$) than typical electron drift times (up to several ms), it provides a precise event trigger. Liquid argon, due to its relatively high density of 1.4 g/cm^3 is a good target that is suitable for rare event searches, such as the detection of neutrino interactions or nucleon decays. It is the most abundant rare gas in air (0.93 %) and a by product of the liquid air industry. Therefore, LAr is relatively cheap and available in large quantities. The contamination of electronegative impurities in commercial LAr is about 2 ppm requires further purification by more than three orders of magnitude is required. The only drawback of the use of liquid argon is the necessity of a careful handling, as it is a cryogenic liquid with a boiling point of 87 K at atmospheric pressure. A summary of the most relevant parameters of LAr as detector medium is presented in Table 2.1.

Table 2.1: Physical, chemical, and thermodynamical properties of argon [1]

Atomic number Z, standard atomic weight	18, 39.948g/mol
Boiling point at 1 atm	87.3 K
Triple point	83.81 K, 0.689 bar
Liquid density at boiling point	0.389 gm/cm^3
Mean excitation energy	188 ev
Average ionization energy W_{ion} (1 Mev e^-)	23.6 ev
Average energy for photon emission W_{ph}(1 MeV e^-)	24.4 eV
Average energy loss for mips $\langle dE/dx \rangle$	1.519 MeV cm^2/g
Radiation length X_0	19.55g/cm^2
Nuclear interaction length X_0	119.7 gm/cm^2
Scintillation wavelength	128 nm
Dielectric constant ϵ_r	1.5

2.2 Liquid Argon Time Projection Chamber (LArTPC) Working Principle

A TPC consists of two parallel planes, cathode and anode, separated by the drift gap that can range from a few *millimeters* to several *meters* depending on the field of application of the device. While the anode is connected to ground , the cathode is biased to a high negative electric potential to set up an electric field within the detector active volume. The field strength is typically of the order of several 100 V/cm for the largest drift gaps and up to a few 10 kV/cm for the smallest ones. To guarantee uniformity of the field across the entire sensitive detector volume, equally spaced field-shaping electrodes are installed in between the anode and the cathode, properly biased in their electric potential with respect to one another. The anode is given by the sensing plane which is where the detector output signals are formed and registered by means of a segmented read-out, consisting of two or more wire planes oriented along different directions.

An ionizing particle traveling a LArTPC creates pairs of positively charged argon ions Ar^+ and quasi free electrons e^- along its path (ionizing track). Instead of being ionized, an argon atom may be raised to an excited state, which eventually leads to the emission of argon scintillation light during its de-excitation. Right after creation, an electric field depends on the number of electron-ion pair recombinations, resulting in the emission of more scintillation light. Liquid argon is transparent to its own scintillation light. It can thus be measured by photo detectors as a trigger, to provide a precise event time stamp t_0 and to gain additional information about an event to facilitate its reconstruction. The residual electrons and argon cations, left after recombination, are separated by the electric field forcing them to drift toward the anode or the cathode, respectively. The integrity of the original ionization track is kept during the drifting process because of the high uniformity of the electric field.

During the drift, two physics processes have an impact on the detector performance. First, the drifting electrons are subject to longitudinal (along the drift direction) and transverse (perpendicular to the drift direction) diffusion, i.e., they do not strictly keep their positions relative to one another, but rather they disperse. This limits the spatial resolution of the device. Second, electronegative impurities, such as oxygen and water molecules dissolved in the sensitive liquid argon volume and tend to attach to the electron reducing the amount of charge drifting towards the read-out. Consequently, impurities diminish the detector output signals and hence one is interested in keeping their concentration in the device as low as possible. At the sensing plane, the electrons are registered by the XY-segmented read-out and the signals produced are subsequently amplified electronically. In addition to measuring the XY coordinates, the electron arrival times are recorded. The event time stamp t_0, can be calculated from the measurement of the scintillation light. The actual drift time t_d can be calculated from the arrival times and event time. The third spatial coordinate z of the ionization track can be calculated by drift distance and drift time. After doing a thorough detector calibration and applying appropriate corrections for attachment and recombination losses, the number of electrons collected at the read-out plane yields calorimetric information about an event.

2.3 Energy Dissipation in a Liquid Argon

The energy of particle traversing a medium is dissipated in different ways [21]. Hadrons, such as the neutron, lose their energy by the short-range strong interactions with nuclei of the medium. The electrically charged hadrons also take part in electromagnetic interactions described further below. Neutrinos and anti-neutrinos crossing the detector, can be absorbed by the nuclei of the medium in weak interactions.

Photons or γ-rays lose their energy via the processes of photoelectric absorption, Compton scattering, and pair production. In the process of photoelectric absorption, an incoming photon fully transfers its energy E_γ to one of the shell electrons of an atom. The electron is removed from the shell and its final state kinetic energy $E_{kin} = E_\gamma - E_B$, where E_B denotes its initial atomic binding energy. Compton scattering describes the process where the incoming photon scatters an electron. Only part of E_γ is transferred to the electron and the photon is not absorbed but its wavelength is increased and its direction of flight changes. The process of pair production may only occur if $E_\gamma > 2m_e$ with m_e being the mass of an electron or a positron. The photon produces an electron-position pair in the presence of a spectator nucleus needed to fulfill the conservation momentum law. Which of the three processes dominate depends mainly on the target medium (proton number Z) and on E_γ. Roughly, the interaction cross-section dependences of photoelectric absorption, Compton scattering, and pair production on energy $\sigma_{abs} \approx Z^5/E_\gamma^{7/2}$,$\sigma_{CS} \approx Z/E_\gamma$

and $\sigma_{PP} \approx Z^2 ln(2E_\gamma)$ respectively, the latter with a threshold of $E_\gamma > 2m_e$ [22].

The amount of charge produced by ionization is directly related to the energy deposited in the argon. The conversion factor is given by the value W_i, but recombination and electron attachment losses must be taken into account. The energy deposited per unit track length dE/dx, also known as linear energy transfer (LET), is an important quantity for particle identification and can be precisely measured in LArTPCs. For moderately relativistic heavy ($m \geq m_\mu$) charged particles, the Bethe-Bloch formula, equation 2.1, provides a good description of dE/dx [21].

When a moderately relativistic charged particle travels through the detector medium it loses its energy via single collisions with the electrons of the atoms. The mean rate of energy loss per unit length $-\langle dE/dx \rangle$ for particles with charge ze in the region 0.1< β_γ <1000 is described with an accuracy of a few % by the Bethe equation 2.1.

$$-\langle dE/dx \rangle = Kz^2 \frac{Z}{A} \frac{1}{\beta^2} \Big[\frac{1}{2} ln \frac{2m_e c^2 \beta^2 \gamma^2 T_{max}}{I^2} - \beta^2 - \frac{\delta(\beta_\gamma}{2} \Big] \tag{2.1}$$

Here the unit of the energy loss is $MeVg^{-1}cm^2$, K =0.307 $MeVg^{-1}cm^2$, m_e is the electron mass, and T_{max} is the maximum energy that can be transferred from the traversing particle with mass M to a single electron with mass m_e:

2.4 Recombination Mechanism

A fraction of the electron-ion pairs created during the ionization process in argon are not separated fast enough by the applied electric field and recombine. A variety of models exist [23] to describe these processes, but they are not yet entirely understood. After thermalizaion through collisions with particles of the surrounding medium (within 1 -2 ns) [24], the quasi free electrons created during the ionization process may remain close enough to an ion to be recaptured. The fraction of electron-ion pairs that recombine is strongly dependent on the applied electric field. With an increasing field strength, the Coulomb force separating ions from electrons gets larger and hence there is a smaller chance for recombination. The dependence of the recombination fraction on the electric field strength and on the specific energy loss dE/dx of the ionizing particle is described by a liquefied argon saturation curve shown in Figure 2.3.

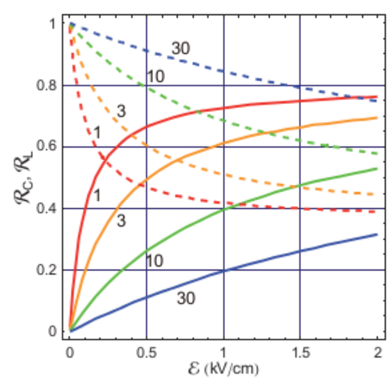

Figure 2.3: The recombination factors for charge (solid lines) and light (dashed lines) as functions of the electric field strength. R_C and R_L denote the collected charge and light at the given electric field divided by respectively the charge collected at infinite field and the light collected at zero field. The number that label the curves denote the specific energy loss dE/dx of the particle in units of minimum ionizing particles [25].

In 1938, Onsager proposed that recombination mainly happens through re-attachment of the electron to its parent ion due to an attractive Coulomb force [26]. A different approach was chosen by Jaffe in 1913 [27]. His model is based on a columnar theory meaning that recombination is expected to depend on collective effects, i.e. on the charge density of electrons and ions within a cylinder along the ionization track. Instead of recombining only with its parent ion, an ionization electron may recombine with any other of the nearby ions. Consequently, the fraction of electron-ion pairs is subject to recombination would also depend on the ionization density and on the type of particle that passes through the medium. The column of electrons and ions evolve as a function of time due to diffusion and to the applied electric field which separated negative from positive charge carriers. During this process, an electron may be captured by one of the nearby ions and the charge left after recombination is described by

$$Q = \frac{Q_0}{1 + q_0 F(Esin\phi)} \tag{2.2}$$

Where Q_0 denotes the total ionization charge before recombination, q_0 is the initial density of electron-ion pairs and F is a function that depends amongst other on the electric field strength E, the angle ϕ between electric field, and ionization track as well as other parameters that describe diffusion. The fraction of charge that does not recombine is given by $R = Q/Q_0$. The Jaffe model assumes the same drift speed for ions and electrons and their mobilities are regarded as constants.

Calculation of the average ion-ion and the electron-ion distances in liquid argon, one can evaluate the relevance of recombination (Onsager model) compared to the columnar effects described by jaffe. By knowledge of W_i and dE/dx in liquid argon, the average distance between ions is calculated to be of the order of 10 to 50 nm depending on the type of the ionizing particle. By contrast, electrons travel distances of about 1000 nm before thermalization [28] which is not only much larger than the distance between neighboring ions, but is about ten times the Onsager radius. Thus, one expects recombination to be disfavoured and that collective effects play an important role during this process. Experimental data indicates that the fraction of electron-ions pairs that recombine depends on the ionization density [28]. The curves shown in Figure 2.3 originate from a reliable fit of the columnar model to experimental data. For higher dE/dx, the density of electron-ion pairs along the track is higher and thus a larger fraction recombines.

Thomas and Imelas [26] reformulated the Jaffe columnar equation by assuming diffusion and ion mobility to be zero. They model the cylindric column by a box that contains a uniform distribution of charge (box model). Typically, the Jaffe model is approximated by means of Birks law [29] , which was originally used to describe quenching effects in scintillators and applied either in the form

$$Q = A.\frac{Q_0}{1 + k_E/E} \tag{2.3}$$

or

$$Q = A.\frac{Q_0}{1 + K_q dE/dx} \tag{2.4}$$

where k_E and k_q are fit parameters. A is added to match the experimental data better in low field region [30]. The parameter values that were found by the ICARUS collaboration [30] fitting Equation 2.4 to the data are

$$A = 0.800 \pm 0.003 \tag{2.5}$$

and

$$k_E = 0.0486 \pm 0.0006 \tag{2.6}$$

To obtain calorimetric information for an event in a LArTPC, the collected charge must first be corrected for electron attachment losses caused by impurities, and second for recombination. The latter is done while transforming the charge collected at the TPC read-out, ΔQ, corrected for attachment losses, into the equivalent amount of energy ΔE

$$\Delta E = \frac{\Delta Q}{R} W_i \tag{2.7}$$

or

$$\frac{dE}{dx} = \frac{dQ/dx}{R} W_i \tag{2.8}$$

where dQ/dx and dE/dx are the residual charge after recombination and the energy deposited per unit track length, respectively. By means of equation 2.4,

$$\frac{dE}{dx} = \frac{dQ/dx}{A/W_i - k.(dQ/dx)/E} \tag{2.9}$$

where k is given by k_E normalized to the density of liquid argon $k = k_E/\rho_A r$. dQ/dx is in units of number of electron-ion pairs per unit track length.

Recombination occurs either directly via $Ar^+ + e^- \rightarrow Ar^*$, followed by de-excitation of the Ar^* via emission of VUV photons or through non-radiative relaxation (heat), or through a triple collision of the argon cations with the surrounding argon atoms. This latter is very efficient due to the high density of the liquid. It results in the formation of an ionic excimer state Ar_2^+ [31]

$$Ar^+ + 2Ar \rightarrow Ar_2^+ + Ar \tag{2.10}$$

A third argon atom has to take part in this interaction to guarantee momentum conservation. An excimer describes a compund of two atoms (molecules) that is strongly bound only in its excited states. Recombination happens with the ionic excimer Ar_2^+ which leads to highly excited state Ar^{**} of an argon atom

$$Ar_2^+ + e^- \rightarrow Ar^{**} + Ar \tag{2.11}$$

Again, the highly excited Ar^{**} relaxes to the first excited state Ar^* by two mechanisms. The first excited states subsequently de-excite under the emission of light. As a result, one expects the light yield to be higher when a larger fraction of electron -ion pairs recombines and hence, at a given electric field strength, the light yield increases with higher dE/dx. This anti correlation behavior between collected charge and light is visible, Figure 2.3.

2.5 Scintillation Mechanism in Liquid Argon

Figure 2.4 gives a simplified picture of the two major scintillation mechanisms that occur in liquid argon. Further mechanisms are discussed in [32]. The interactions that take place in a first step are direct excitation by the ionizing radiation and recombination of the electron-ion pairs. In both cases, the intermediate state is given by an argon atom in its first excited state Ar^*. In triple collisions with surrounding argon atoms, the excited argon atom can change its electronic configuration and form an excimer Ar_2^*.

$$Ar^* + 2Ar \rightarrow Ar_2^* + Ar \tag{2.12}$$

The excimer is either bound in the singlet state ${}^1\Sigma_u^+$ or in the triplet state ${}^3\Sigma_u^+$ with different life times after which de-excitation occurs [32].

$$Ar_2^*({}^1\Sigma_u^+) \rightarrow Ar_2({}^1\Sigma_g^+) + \gamma \rightarrow 2Ar + \gamma \tag{2.13}$$

$$Ar_2^*({}^3\Sigma_u^+) \rightarrow Ar_2({}^3\Sigma_g^+) + \gamma \rightarrow 2Ar + \gamma \tag{2.14}$$

The singlet transition to the ground state $Ar_2({}^1\Sigma_g^+)$ of the dimer is fast ($\approx ns$) while the triple transition to $Ar_2({}^3\Sigma_g^3)$ is suppressed and therefore slow ($\approx \mu s$). As a result, the scintillation light in liquid argon has a slow and a fast component. The ratio of the intensities of the two components depends on the ionization density and hence on the type of particle that ionizes the medium. The decay of both, triplet and singlet states, lead to a main emission peak at a wavelength of roughly 128 nm with a spectral width of 7 nm to 10 nm [33].

Considered simply, the ground states $Ar_2({}^1\Sigma_g^+)$ and $Ar_2({}^3\Sigma_g^+)$ are repulsive only and very short-lived [32]. They almost immediately separated into two argon atoms. As a result, there is no resonant re-absorption of the scintillation photons and argon is transparent at these wavelength.

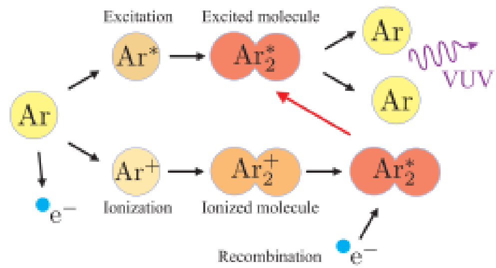

Figure 2.4: Simplified picture of the main scintillation mechanism in liquefied argon.

2.6 Electron Attachment Losses

The removal of impurities from noble gases and liquids has already been studied extensively [34]. The main contaminants of concern in these media are atoms or molecules with a high electro-negativity as they have a larger tendency to attach an electron to form a negative ion. Typical contaminants present in LArTPCs are oxygen O_2, water H_2O, or carbon dioxide CO_2 . The attachment of electrons to atoms and molecules happens in various ways [35]. Radiative attachment is where a neutral atom or molecule binds an electron to form a negative ion under the emission of a photon. This process is negligible in liquid argon [35]. A second way how quasifree electrons can be temporarily bound is dissociative attachment. A molecule XY captures an electron to dissociate into X and Y^- , either via an intermediate excited XY^* or a negatively ionized XY^- state. In liquefied argon, the dominant branch for electron attachment is a three-body process was first described by Bloch and Bradbury [36] and later refined by Herzenberg [37]. Electron attachment to a neutral atom or molecule XY proceeds in two stages. First, the XY captures an electron to produce a vibrationally excited temporary negative-ion state $(XY^-)^*$

$$e^- + XY \longleftrightarrow (XY^-)^* \tag{2.15}$$

After a finite lifetime, the $(XY^-)^*$ either autoionizes back into a free electron and the neutral molecule or it collides with a third partner, usually an atom or molecule of the host medium and thereby loses its excess vibrational energy

$$(XY^-)^* + Ar \rightarrow XY^- + Ar \tag{2.16}$$

The rate of electron removal from a charge cloud consisting of a number $N_e(t)$ of elctrons at time t is is appropriately modelled by [35]

$$\frac{dN_e}{dt} = -k_{tot}.N_e(t) \tag{2.17}$$

where $k_{tot} = \sum_i k_i$ with the k_i describing the probability for an electron to be attached to an atomic or molecular impurity of type i. The k_i are directly proportional to the number densities n_i of the corresponding kind of impurities. By integrating Equation 2.4, one finds that the number of ionization electrons remaining after a time t is given by

$$N_e(t) = N_0.e^{-k_{tot}t} = N_0.e^{-t/\tau} \tag{2.18}$$

Where N_0 denotes the initial number of ionization electrons left after recombination, i.e. at t=0 here. A rule of thumb relating the level of oxygen equivalent impurities to the characterstics time constant τ (charge lifetime) is given by [2.30]

$$\rho_{O_2}[ppt] \approx \frac{300}{\tau[ms]} \tag{2.19}$$

Where ppt stands for parts per trillion (10^{-12}).

The removal of drifting electrons due to impurities diminishes the charge that can be read out at the sensing plane and thus reduces the signal-to-noise ratio of the detector. Hence, the level of impurities has to be kept as low as possible. Moreover, to obtain calorimetric information, one must have knowledge of the argon purity or, equivalently of τ, to correct for the attenuation of the signals.

2.7 Wireplane read-out and Signal formation

A wire plane is an array of thin, conductive, parallel wires separated by ≈3 mm. To realize segmentation along different coordinates, the read-out configuration consists of two or three wire planes of different orientations separated by a small gap of up to a few mm. The left hand side of Figure 2.5 shows the projections $y-z$ and $x-z$ of a read-out configuration with two wire planes. The lower one with wires oriented along the y axis is labeled X while the upper one is named Y and has wires along the x axis.

An electron generated in the detector volume follows the applied uniform drift field E_0 and approaches the first wire plane X which is set to ground potential. To make sure that the electrons are not collected already by the first wire plane, the Y grid must be biased to a positive potential to produce an electric field $|\mathbf{E_1}| > |\mathbf{E_0}|$ between the two planes. By setting up a field of an appropriate strength, the field lines terminate only on the wires of the Y plane and hence the X plane appears to be fully transparent for the drifting electrons (see Figure 2.5, left). The transparency condition for a wire grid consisting of equidistant wires and separating two regions i and j with electric field strength of E_i and E_j respectively is given by [38]

$$|\mathbf{E_i}| > \frac{1+\rho}{1-\rho}|\mathbf{E_j}| \tag{2.20}$$

where $\rho = 2\pi r/d$ with r and d the wire radius and the wire spacing respectively.

The moving charge carriers approaching the wire planes X induce currents in the wires located at the corresponding spatial coordinates. Once the electrons have passed through the wire plane, the electric current in the wires is reversed. That is why a bipolar signal is observed from the wires of the X plane (see Figure 2.5, right). As long as the transparency condition is met, none of the drifting charge carriers are collected at the wireplane X and the read-out is said to be non-destructive or operated in induction mode.

At the Y wire plane the electrons are finally collected (collection mode, destructive read-out) which is why the induced signals from the wires of the Y plane are unipolar. To resolve ambiguities in the event reconstruction, a setup with three wire grids U, V, X (two in induction and one in collection mode) is usually chosen. The two induction planes U and V are at specific angles with respect to the collection plane. Sometimes, the U plane is not instrumented and only serves as a shielding grid to avoid signal induction on the V plane before the electrons enter the read-out zone. Such a configuration ensures to a well-shaped signal from the V plane.

For a wireplane configuration typically set up for LArTPCs, a track induced by a minimum ionizing particle leads to about 6000 electrons per wire at the read-out [40]. This corresponds to about one fC of charge. To process and digitize such signals with

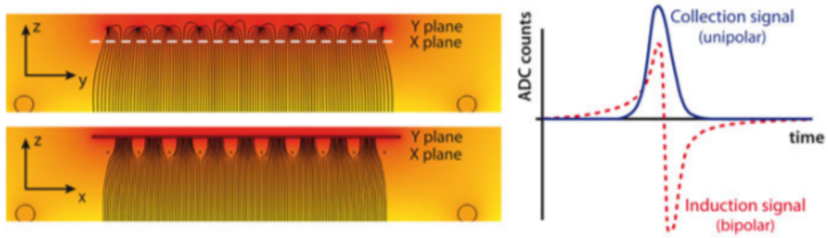

Figure 2.5: *Left:* Typical wireplane read-out of a LArTPC [39]. The X plane is at ground potential and in the non-destructive induction mode, i.e. fully transparent for the drifting electrons. This is achieved by setting the Y grid to an appropriate positive potential. The electric field lines terminate on the Y plane which is thus in the destructive collection mode. *Right:* Examples of bipolar induction (dashed line) and unipolar collection (solid line) signals as they result from the X and Y planes, respectively.

an ADC (analog-to-digital converter), an intermediate electronic pre-amplifier stage is necessary.

2.8 Status of Current Liquid Argon Detectors

The technology of LArTPC, first proposed by Professor Carlo Rubbia in 1977, was conceived as a tool for completely uniform imaging with high accuracy of very massive volumes (several thousand tons). ICARUS is the first large-scale detector, exploiting this detection technique [41]. The ICARUS program uses a LAr detector for studies of neutrinos from CNGS beam. The ICARUS detector, filled with 600 tons of liquid argon, started data taking in 2010. The detector was placed at the undeground laboratory in Gran Sasso. The read-out chambers (two TPCs for each half-vessel) are mounted on the internal walls with the cathode at the centre, to maximize the LAr sensitive volume (corresponding to about 480 ton in mass). The read-out chamber scheme consists of three parallel planes of wires (horizontal, +60 and −60 degrees). Information is read both by electric charge induction on the first two readout planes encountered by drifting electrons and by electric charge collection on the last readout plane. The signals from the three wire planes, together with measurement of the drift time, provide a full 3-D image reconstruction of the event. The schematic representation of a time projection chamber is shown in Figure 2.6.

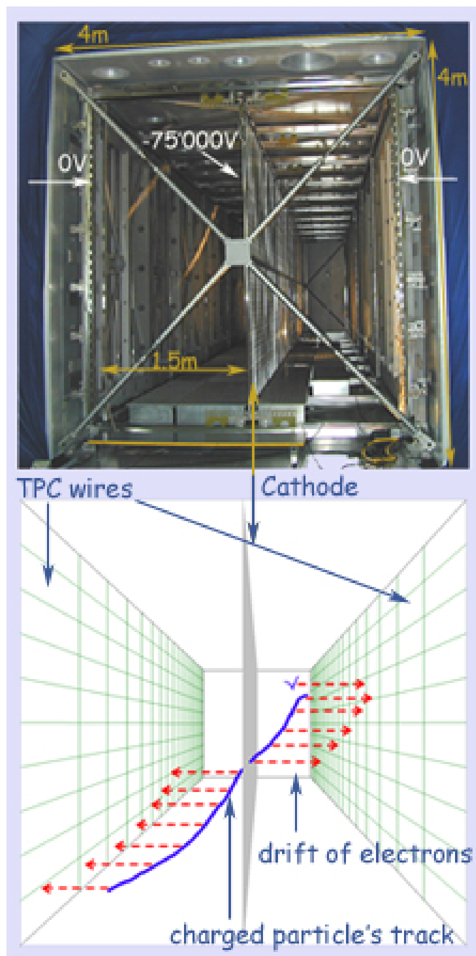

Figure 2.6: Schematic representation of a single module of the ICARUS detector and its functionality [41].

ArgoNeuT was another liquid argon experiment ar Fermi lab [42] that used liquid argon to detect and record neutrino interactions. It contained 175 L of liquid argon in the TPC, which consists of three wire planes oriented at 60^o relative to one another. Each plane has 240 wires spaced 4 mm apart. ArgoNeuT's[Figure 2.7] neutrino source was the NuMI (Neutrino at the Main Injector) beam. The beam passes through the MINOS near and far detectors, positioned at 1km and 735 km from the target at Fermilab. ArgoNeuT was located at Fermilab upstream of the MINOS near detector, and is calibrated using muons that traverse the chamber and penetrate several layers into MINOS.

Figure 2.7: ArgoNeuT detector [42].

The **MicroBooNE** experiement is currently operating a 170-ton LArTPC located in the Booster neutrino beam line at Fermilab [43]. It is currently the largest LArTPC operating in the U.S.The TPC (Figure 2.8) consists of a cathode plane on one side, a field-shaping cage around the drift perimeter, and three planes of wires of the opposite end to record the signals from the drifting ionization electrons. The MicroBooNE detector was filled with liquid argon in the summer of 2015. The argon was successfully purified using the MicroBooNE filtration, reciruculation, and purification system. MicroBooNE saw first cosmic ray tracks in the TPC in August 2015 and started collectring neutrino beam data in October 2015.

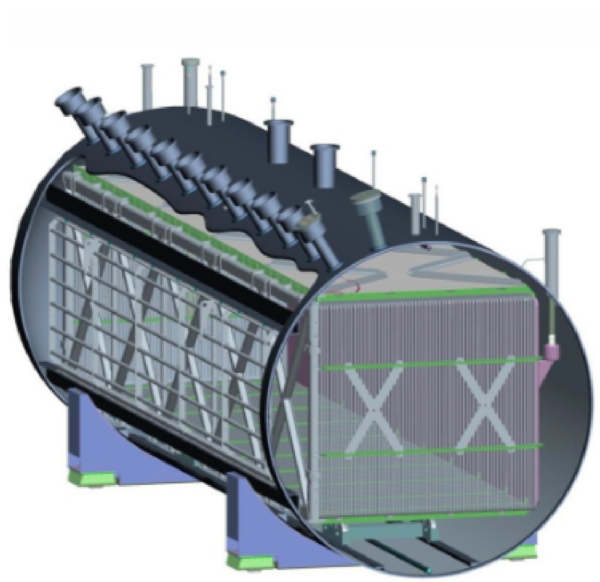

Figure 2.8: The MicroBooNE detector [43]. The high voltage feedthrough enters on the right and supplies voltage to the cathode plane. One side of the field cage can be seen on the face of the cut-away (supported by the "X" braces). The sense and induction wires are on the left side of the vessel. Behind the wire planes is the support structure for the PMT array (not shown).

Chapter 3

CAPTAIN experiment

3.1 Introduction

The Cryogenic Appartus for Precision Test of Argon Interactions with neutrinos (CAPTAIN) began as a Los Alamos National Laboratory (LANL) Directed Reseach and Devlopment (LDRD) project and has now evolved to be a multi-institutional research collaboration [19]. The scientific focus of the CAPTAIN program is to make measurements important for the development of the Deep Underground Neutrino Experiment (DUNE). DUNE is a broad scientific program being developed in the United States as an international partnership. It consists of an intense neutrino beam produced at FNAL, a highly capable set of neutrino detectors on the FNAL campus, and a large underground liquid argon TPC at Sanford Underground Research Facility (SURF), giving a 1300 km oscillation baseline. The high-intensity neutrino beam will allow high precision measurements of neutrino and antineutrino mixing separately, enabling detailed studies of neutrino oscillations, including measurements of the mass hierarchy, CP violation, and non-standard neutrino interactions (NSI). In addition to serving as a far detector for the long-baseline neutrino physics program, the large underground detector enables a broad scientific program that includes searches for nucleon decay mediated by beyond the standard model physics, the study of neutrinos from galactic supernova bursts, indirect searches for the annihilation products of dark matter particles and the detailed study of atmospheric neutrinos. The CAPTAIN program impacts several of the topics that make up the DUNE physics program via two fronts of study: low energy neutrino physics and medium energy neutrino physics.

Liquid argon detectors will have excellent sensitivity to ν_e from supernova via the CC interaction on 40 Ar,$\nu_e + {}^{40}Ar \rightarrow e^- + {}^{40}K^*$. In principle, this is a taggable interaction, for which the deexcitation γ from ${}^{40}K^*$ can be observed. The $\bar{\nu}_e$ interaction, $\bar{\nu}_e + {}^{40}Ar \rightarrow e^+ + {}^{40}Cl^*$, will also occur and can be tagged via the pattern of γ. NC excitations ($\nu_x + {}^{40}Ar \rightarrow \nu_x + {}^{40}Ar^*$) are also possible and 200 events are expected in 34 KT at 10 kpc. Finally, there will be elastic scattering of neutrinos on electrons. Large liquid argon detectors suitable for supernova neutrino detection are primarily large TPCs, in which ionization charge is drifted by an electric field and signals are collected on wire planes. Using the time of arrival of charge at the readout planes, one can reconstruct a three-dimensional track; particles can be identified by their rate of energy loss along a track. Argon also scintillates, and scintillation photons collected by PMTs enable fast timing of signals and enhance event localization within the detector. Liquid argon TPC detection technology offers good energy resolution and full particle reconstruction, unaffected by Cherenkov threshold. For sufficiently fine wire spacing, millimeter position resolution and very high-quality tracking can be achieved. Energy thresholds as low as a few MeV may be possible. The direction of the scattered electron for elastic scattering can be determined. Understanding the interaction $n + {}^{40}Ar \rightarrow n + {}^{40}Ar^{*}$ is important for supernova neutrino detection. We can study the signature of the Ar^{*} de-excitation to gain insight into detecting supernova neutrinos in the neutral current (NC) channel. We can also better separate the NC signal from the neutron background.

Medium-energy neutrino interactions are poorly understood on any nucleus. There is a dearth of neutrino-argon data in the 1 to 10 GeV neutrino energy regime. DUNE will use data in this energy regime to make high-precision measurements of neutrino oscillation. Irrespective of the source of medium-energy neutrinos (beam or atmospheric), neutrino oscillation studies depend on having well-constrained determinations of three quantities for each neutrino event: the neutrino flavor, the distance from the point of production, and the neutrino energy. In general, CC neutrino interactions in this energy regime will result in a charged lepton, the emission of several hadrons, and a residual nucleus. While charged hadrons will be well-identified and measured, neutrons are harder to measure. They travel some distance from the neutrino interaction vertex and deposit energy via elastic and inelastic collisions with the argon nuclei. The determination of the neutrino energy is therefore a significant challenge and possible systematic limitation to the DUNE neutrino physics program.

Currently, CAPTAIN is conducting a detailed study of neutron interactions with argon as a function of neutron energy up to neutron kinetic energies of 800 MeV. Using these data, the collaboration will develop methodologies to constrain the neutron energy in a neutrino interaction.

3.2 mini-CAPTAIN Detector

The mini-CAPTAIN detector is prototype detector for CAPTAIN. It is a hexagonal shape 1 m across parallel sides with a 32 cm drift. The active mass of liquid argon is 400 kg. The prototype TPC (Figure 3.1) is constructed with FR-4 material and has a wire mesh cathode to allow the photon detection system to capture scintillation light, two induction planes, a collection plane, a wire grid plane to define the first induction plane signal, and a ground plane for the HV return. The order of the planes (as the drifting electrons see them) is grid plane, U induction plane, V induction plane, collection plane, and the ground plane. The plane spacing is 3.18 mm and the wire spacing is 3 mm. The drift field is 500 V/cm and the drift velocity is 1.6 mm/μs. The TPC is composed of two sub assemblies, a field cage and a wire plane assembly. The wire planes are attached to a heavy duty support. The Photon Detection System (PDS) is designed to utilize the scintillation light to aid in event reconstruction, provide timing for non-beam events, and provide a time of flight for neutron beam running. The PDS baseline is 16 Hamamatsu R8520-500 photomultiplier tubes viewing the active region with tetraphenyl butadiene as a wavelength shifter to shift the argon scintillation light (128 nm) to the visible. The field cage has 6.35 mm thick copper clad FR-4 field electrodes with coppaller strips spaced at 1 cm.

To insure that the induction planes are transparent to the drifting electrons, a bias is applied to of the wire planes. The bias is determined by using the transparency condition. All wires are 75 μm CuBe and each plane has 338 wires. The field cage

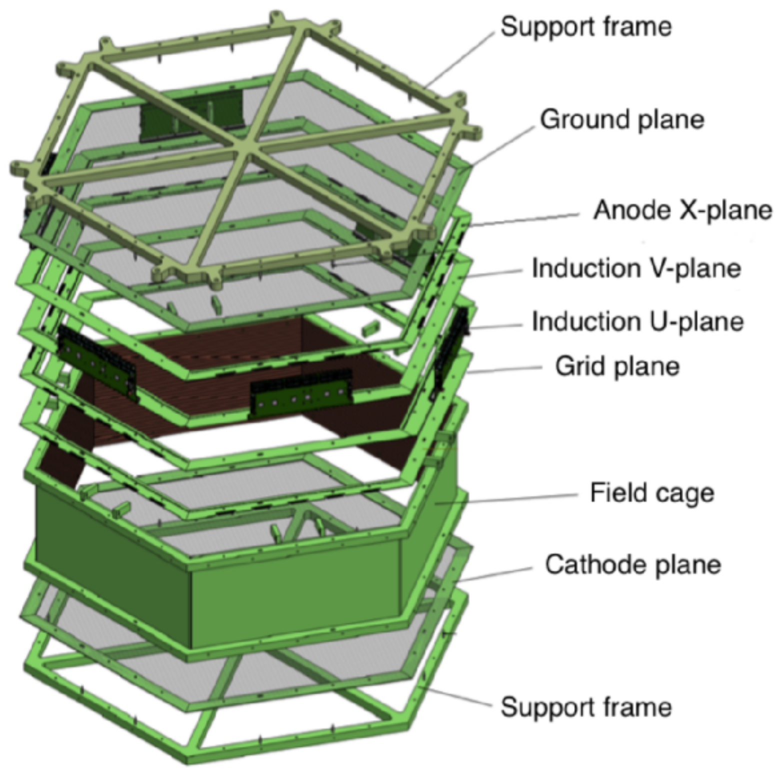

Figure 3.1: 3D model of mini-CAPTAINs time projection chamber (TPC). From bottom to top: the cathode plane is held at -16 kV, the capacitive rings on the field cage is step down in voltage each ring to provide 500 V/cm, the transparent grid plane shapes the field lines, for the following inductive u- and v-planes, and the collection anode plane collects drifting electrons.

and wire plane are shown in Figures 3.8 and 3.3.

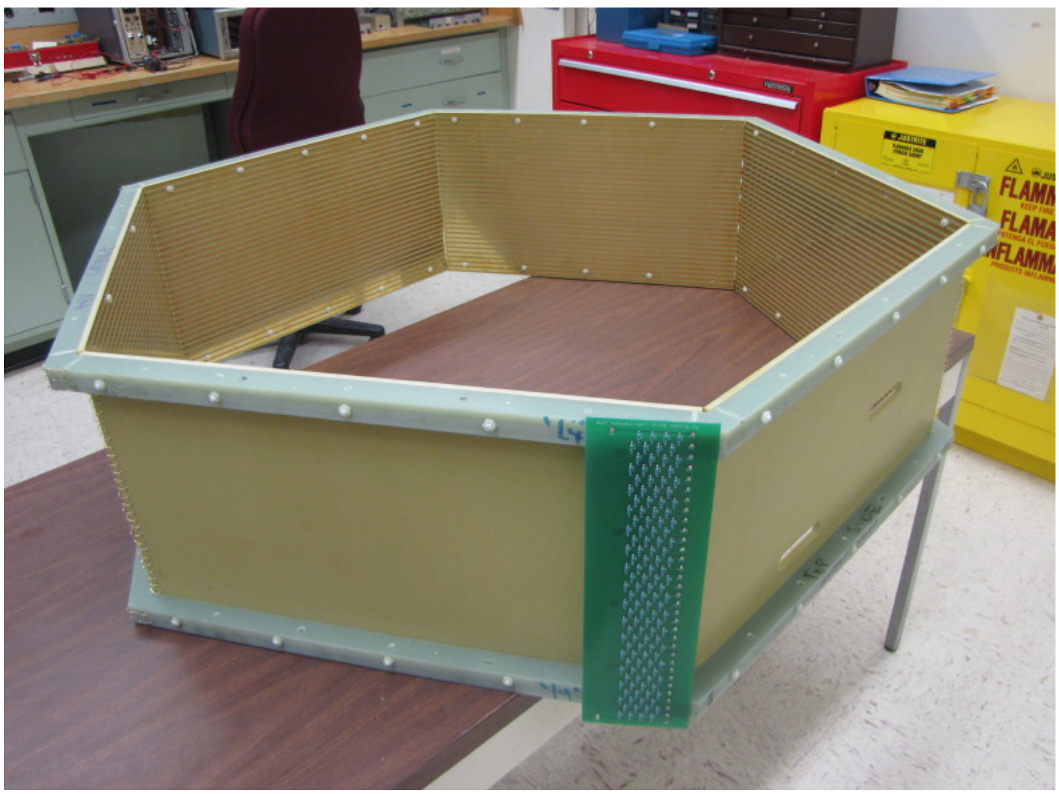

Figure 3.2: Field cage for mini-CAPTAIN.

Figure 3.3: Wire plane of mini-CAPTAIN.

3.3 mini-CAPTAIN Cryostat

The mini-CAPTAIN cryostat is 1700 L vacuum jacketed cryostat. The vacuum jacket is 60.25 inches in diameter, and the vessel is 64.4 inches in height. The vessel is designed with a thin (3/16 inch) inner vessel to minimize heat leak to the argon. All instrumentation and cryogenics are made through the vessel-top head. The vessel also has side ports allowing optical access to laser calibration or other instrumentation. Figure 3.4 shows a schematic of the mini-CAPTAIN cryostat.

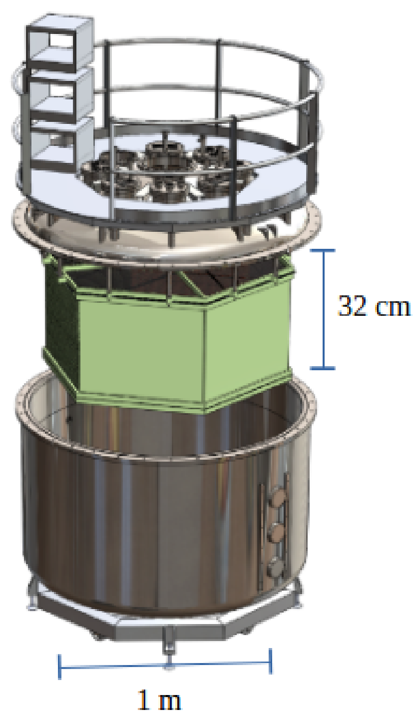

Figure 3.4: mini-CAPTAIN cryostat.

3.4 Cryogenics

LAr serves as target and detection medium for the mini-CAPTAIN detector. The argon must stay in the form of a stable liquid and must remain minimally contaminated by impurities such as oxygen and water. This is to prevent the loss of drifting electrons to these electronegative molecules. It must also stay sufficiently free of contaminants such as nitrogen to avoid absorption of the scintillation light.

The maximum drift distance is 32 cm for mini-CAPTAIN. To achieve a sufficiently long drift-distance for electrons, the O_2 contamination is required to be lower than 750 ppt. The purity received at Los Alamos from industry has an oxygen level of not more than 2.3 ppm. The cryogenics system must receive liquid argon from a commercial vendor, test its purity, and further purify it. Figure 3.5 shows the schematic of cryogenic system. Commercial analytic instruments are used to characterize the oxygen and water contaminant levels in the argon. The dual filter system consists of a bed of molecular sieve (208604-5KG Type 4A) to remove moisture and another bed of activated copper material (CU-0226 S 14 X 28) to remove oxygen. The Figure 3.6 shows the inline filter when it was functional.

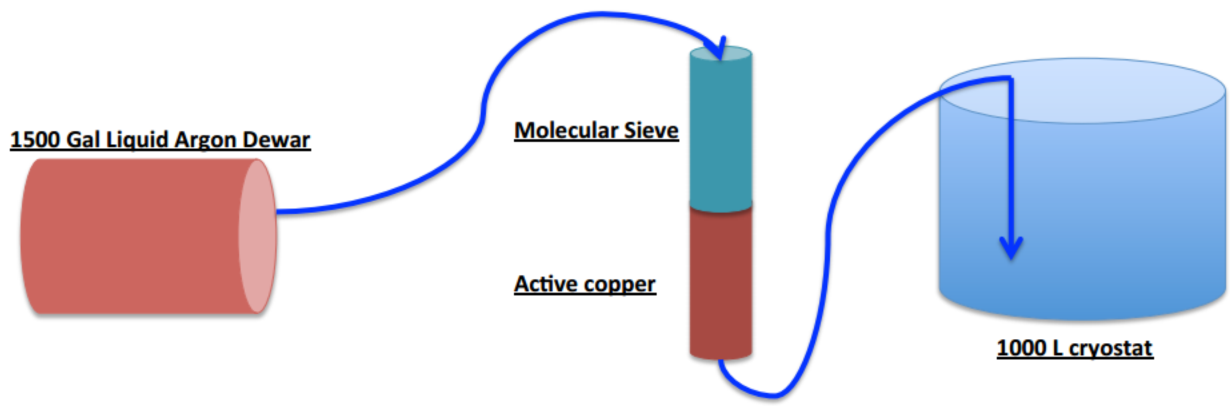

Figure 3.5: Schematic diagram of the cryogenic system.

Figure 3.6: Inline filter during the neutron run.

The inline filter works two ways:

- Water is removed by heating up to 200-315 ^{o}C.

- Oygen is removed by the reaction:

$$2Cu + O_2 \rightarrow 2CuO \tag{3.1}$$

Copper has to be regenerated for continued running. We did this by flowing hydrogen in the sieve.

$$CuO + H_2 \rightarrow Cu + H_2O \tag{3.2}$$

3.5 mini-CAPTAIN Electronics

The electronics chain of mini-CAPTAIN can be broken intro two primary categories- the front end electronics (FEE) and the back-end electronics (BEE) (see Figure 3.7). The FEE includes the electronics on top and inside the cryostat. The remaining BEE electronics process the signal and pass it onto the computers. The data acquisition computer systems can be thought of as as third category, which configures the front-end and controls the collection of data from the back-end. Once powered and configured, both the FEE and BEE can function independently.

The process begins when the computer uses the ASIC configuration board to send an instruction signal to the service card on the front-end electronics. In turn, the service card passes this signal (as well as power) to the ASICs on cold motherboards. The service card also supplies power to the intermediate amplifiers (line drivers).

The ASICs can be configured for four gain-levels and rise-time settings. Without initial configuration, the motherboards do not produce an output. However after initialization, the motherboards are continuously collecting signals from the wire planes and sending them to the intermediate amplifiers. Most initial testing is done with an oscilloscope probe on the differential outputs of the amplifier cards.

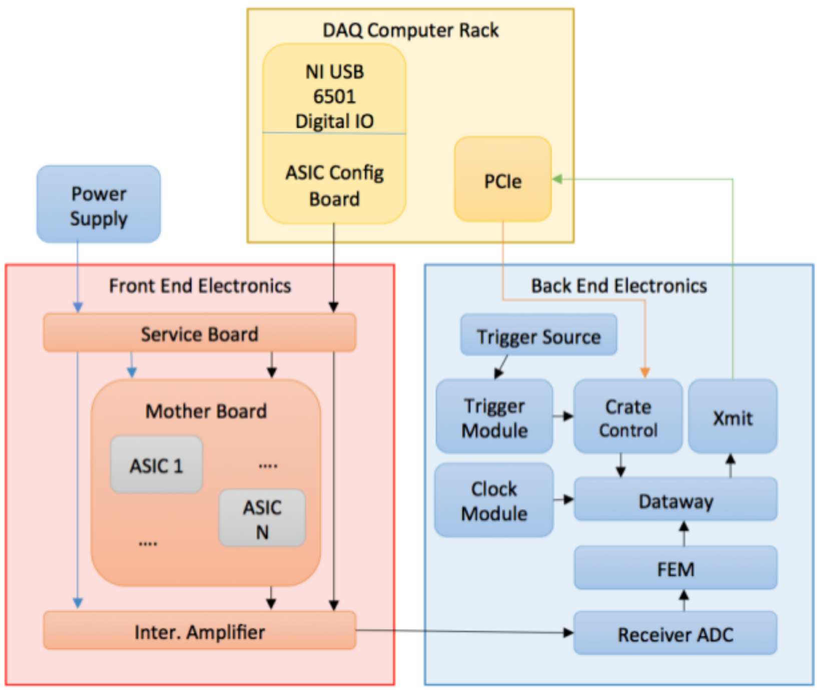

Figure 3.7: Flow diagram of the electronics for the mini-CAPTAIN detector. The electronics can be categorized as a front and back-end. The DAQ computer both configures the ASICs on the mother boards and collects data from the crate FEM cards.

The back-end electronics begins with the receiver ADC. Analogue signal is converted into digital signal and passed to the front-end module (FEM) card for processing. The FEM card runs on a clock and will continuously sample and record the output of the ADC, even if no signal is processed. Without a trigger, this data is simply stored and dumped every cycle. Once a trigger is received through the crate controller, a predetermined sample data size is taken from the FEM memory and passed onto the transmit (Xmit) card. The computer then pulls the data from the xmit card. The crate control can be triggered from both the DAQ computer and the trigger module. The trigger module was designed to take one or more triggers from multiple sources.

Mini-CAPTAIN also has the photon detection system for the measurement of scintillation light. The photons released from a particles interaction is used as the primary trigger source for the both the PDS and TPC data acquisition. The PDS was initially designed to have PMTs on the top and bottom of the TPC. However, during the construction phase, it was deemed less problematic to install all 16 PMTs on the bottom.

3.5.1 Field Cage Assembly

The field cage is a double-sided gold plated copper clad FR4 arranged with 5 mm wide traces separated by 1 cm. A resistive divider chain provides the power for each trace as shown in Figure 3.8. Gold plated jumpers pass the power between each side of the chamber. The divider uses 25 M per centimeter divisions, producing a gradient of 500 V/cm with current of 21 A. One side has two 1 × 5 cm slits for laser access to the active volume. The FR4 support frames held tension on the wire planes during assembly. They also bind the TPC components together as the assembly hangs from the top head.

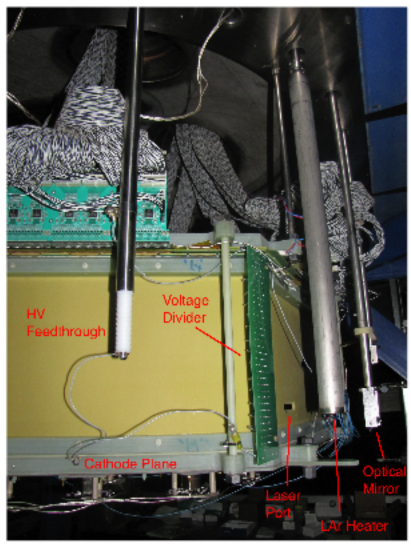

Figure 3.8: View of the field cage assembly. The -16 kV is supplied to the cathode plane from the HV feedthrough.The power the goes through the voltage divider chain, terminating at the top of the cage.

3.5.2 Cold Electronics

Most of the recent liquid argon experiments have made the shift to cold front-end electronics. This minimizes the path length between the signal wires and the preamplifier,reducing the total capacitance seen by the input. The development of cold electronics in LAr detectors is led by Veljko Radeka and Hucheng Chen. In their work, they show that the feasibility and scalability of a LAr TPC design critically depends on the total capacitance limits to the signal-to-noise ratio. Thermal noise from the sense wire is mitigated with the use of copper beryllium material for the wires. The thermal noise is calculated based on the transmission line model of the sense wire. The sense wire noise contributions are equivalent to a third of the wires length. This contribution is only significant at lengths greater than 10 meters if stainless steel is used. Thermal noise is not expected to be a noticeable problem for mini-CAPTAIN.

3.5.3 Back-End Electronics

It would be reasonable to consider the ADC receiver boards and front-end module (FEM) cards as front-end electronics. However, for power and grounding isolation, we found it best to keep them separate and call them the back-end electronics. Each DAQ sub-event builder (SEB) computer controls and reads from its own crate. The DAQ main assembler collects the data from the two SEB machines. The photon detection system VME crate sits on top of the FEE rack, while the power supply, voltage distribution modules, and breakout box are mounted above the DAQ. The clock model sits in its own half-rack behind the FEE power supplies.

Figure 3.9: Electronics racks for mini-CAPTAIN. The rack on the left holds the DAQ computers. The center holds the backend electronics and their power supplies. The last rack holds the power supplies for the front end electronics, as well as the NIM modules for trigger logic.

The TPC readout board receives data through 64 wires. It is setup in two parts: the digitalizing section, which Brookhaven National Lab designed, and the data handling section which Nevis lab electronics handled. The mechanical assembly results in a standard VME 9U card in height with 280 mm depth. The digitizing board is laid out as an 8-layer printed circuit board. The data handling section has a 14-layer printed circuit board. The BNL receiver/ADC board is interfaced with the Nevis FEM (front end module) board as seen in Figure 3.9.

LANL's test-stand was built for complete characterization of the full detector signal readout chain. Test motherboards are supported on the stand below the mock feedthrough. Cold cables run the data up to the intermediate amplifiers. Warm cables run the differential signals to the BEE crates. An interface board transfers ADC data to a Xilinx FPGA evaluation board ML605 for data collection. The test stand proved valuable in both testing the motherboards as well as the FEM cards.

3.6 Scintillator

During the neutron run, we measured the neutron flux with scintillator which was placed upstream of the mini-CAPTAIN detector. The drawing and the picture of the scintillator are shown in Figure 3.10.

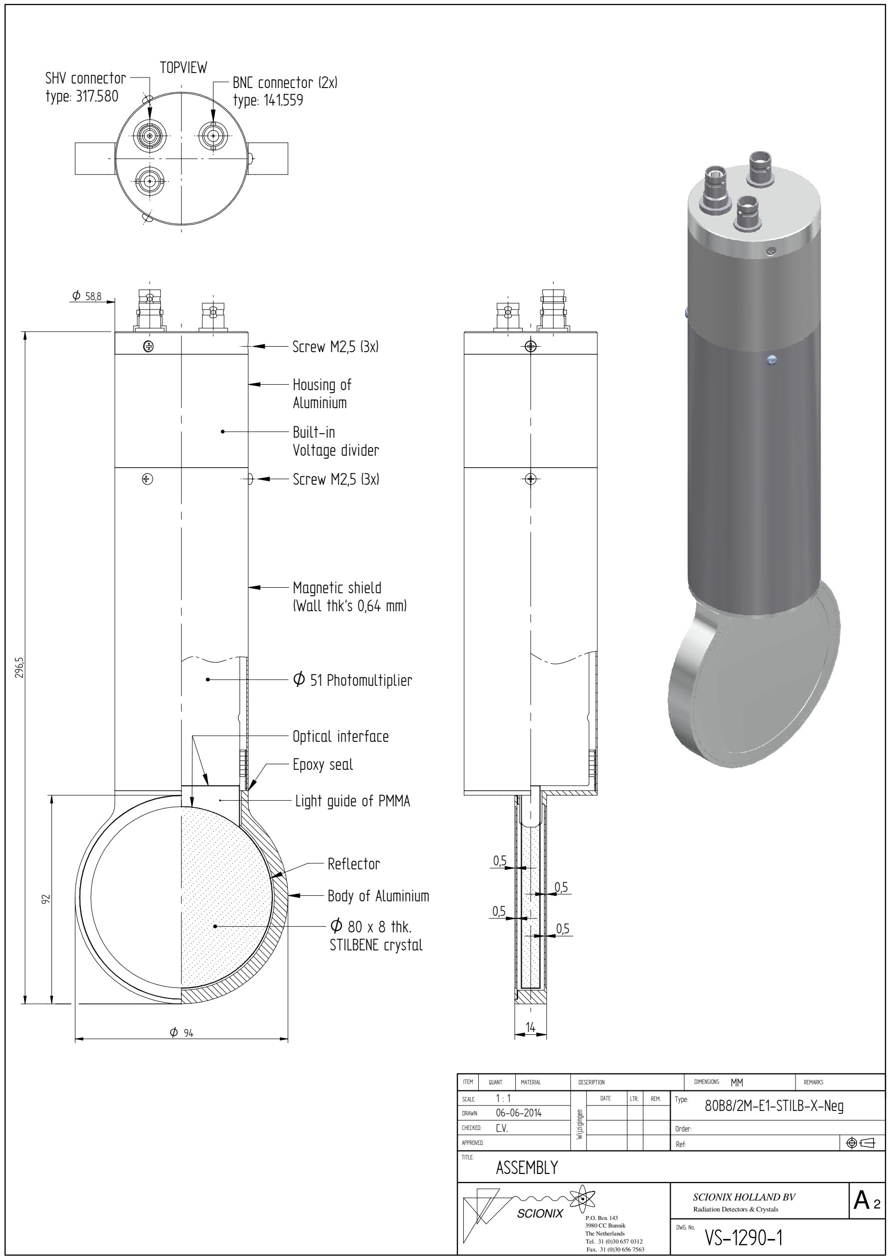

Figure 3.10: The drawing of the scintillator.

The material used in the scintillation is stilbene (diphenylethylene), a molecular organic crystal built of aromatic hydrocarbon molecules. Crystalline stilbene is an organic scintillator used for radiation detection and is well-suited for discrimination between fast neutrons and a gamma-ray background [44]. Neutrons and gammas produce light scintillation in stilbene with significantly different decay characterstics. The 10% to 90 % rise time of the integrated light from all the scintillators is approximately 130 ns when excited with neutrons and approximately 10 ns when excited with gamma rays.

In order to interpret the effective decay time difference of stilbene, consider a proton or electron stopping in the crystal. The incident particle loses energy, dE, in an element of distance, dX, along its track by producing excited molecules M^* and ionized molecules M^+. There are primarily two modes by which the excited molecule decay. These are:

$$M^* \rightarrow M + h\nu \tag{3.3}$$

$$M^* \rightarrow M + heat\ energy \tag{3.4}$$

In the first process, the molecule emits light photons which could ultimately be detected. The second process is quenching where electronic excitaton energy is converted intro vibrational energy. Ionized molecules formed by the incident particle must undergo a delayed recombinaiton process,

$$M^+ + e^- \rightarrow M^* \tag{3.5}$$

The excited state molecule, M^* formed by recombination can now decay by either

3.3 or 3.4. The recombination process is slow. According to Birks, the light output is a function of the initial ionization and excitation density i.e. number of M^+ and M^*per unit path length along the track in the scintillator. For proton excitation, where the ionization and excitation density is high, the excited molecules find themselves in an environment which offers additional modes of quenching. Thus, for protons, less light is emitted initially (fast components) than for electrons which have a considerably smaller ionization and excitation density. Near the end of the path where dE/dX is greatest, more M^+ molecules are formed and hence recombine. However, M^*molecules are born into an environment where the excitation density is much less than it was initially so the molecules are most likely to emit photons rather than be quenched. This slow component decay time is essentially the recombination time. For heavily ionizing protons, more light would be emitted in the long component than for electrons [45].

3.7 mini-CAPTAIN Commissioning

There were three phases to the mini-CAPTAIN commissioning, they are warm testing, liquid nitrogen,and liquid argon. We tested the electronics in vacuum and atmosphere with an oscilloscope ahead of nitrogen filling. In June 2014, we began a liquid nitrogen test of the system. This testing served mostly as an electronics test, but was also used to study some cryogenic issues. The motherboards were under vacuum for over a month prior to the liquid argon fill. There were no indications of motherboard degradation over that time period. Isolation transformers were used to improve the source power. The identified sources of noise can be broken into following categories: power-source ripple, radio-frequency signal pickup, and common mode noise.

The laser data was taken in the second and third liquid argon run cycles. Figure 3.11 shows the first confirmed laser track in mini-CAPTAIN during the third liquid argon cycle testing. This proved that mini-CAPTAIN could achieve purity good enough to observe tracks.

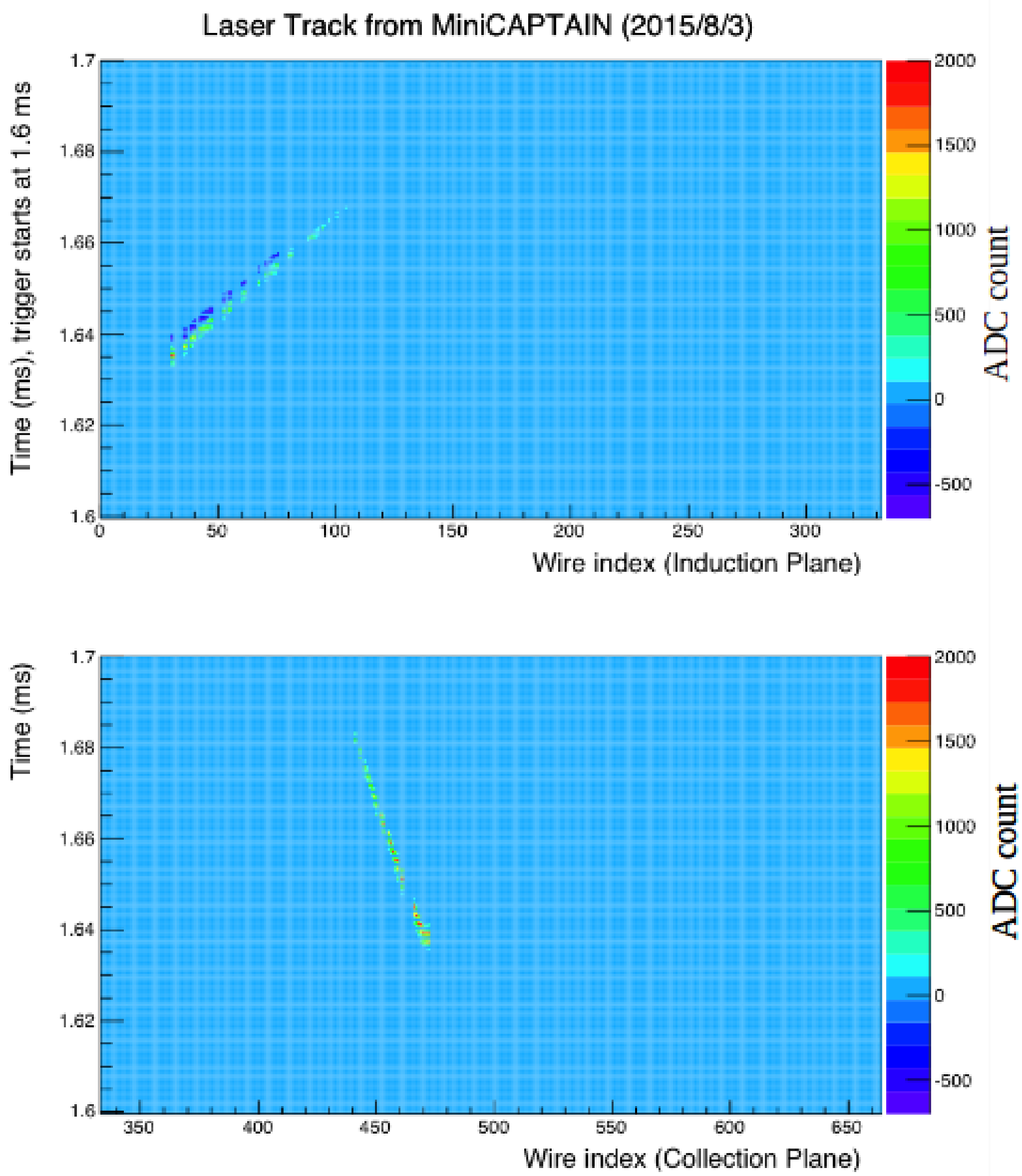

Figure 3.11: First confirmed laser tack found during the commissioning of mini-CAPTAIN. X-axis is wire index and Y-axis is time in ns. Color represents the ADC counts.

Chapter 4

Photon Detection System

4.1 Photomultiplier Tube : Basic Working Principle

A photomultiplier tube is a vacuum tube consisting of an input window, a photocathode, focusing electrodes, and electron multiplier, and an anode usually sealed into an evacuated glass tube. Figure 4.1 shows the schematic construction of a photomultiplier tube.

Light enters a photomultiplier tube, is detected, and produces an output signal through the following processes.

- Light passes through the input window.

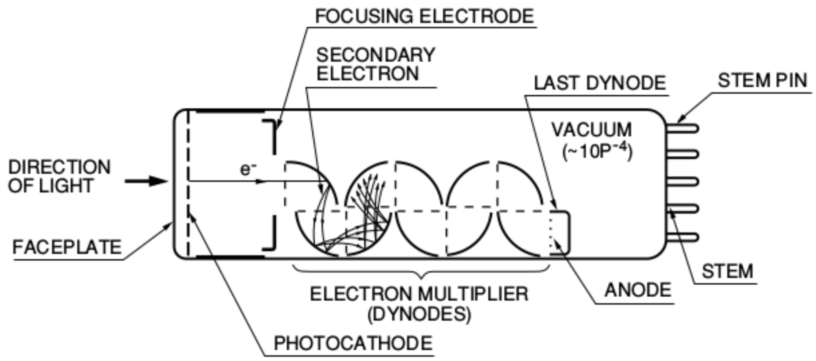

Figure 4.1: Photomultiplier tube [46].

- Light excites the electrons in the photocathode so that photoelectrons are emitted into the vacuum.

- Photoelectrons are accelerated and focused by the focusing electrode onto the first dynode where they are multiplied by means of secondary-electron emission. This secondary emission is repeated at each of the successive dynodes.

- The multiplied secondary electrons emitted from the last dynode are finally collected by the anode.

4.2 Scintillation in Liquid Argon

Charged particles passing through the LAr produce both scintillation and Cherenkov photons, with the isotropically emitted scintillation light dominates by a factor of five. Both sources can be detected within the detector, but the mini-CAPTAIN light collection design optimizes the measurement of the scintillation light.

A MeV of energy loss by a minimum-ionization particle (MIP) results in the production of approximately 24,000 scintillation photons with wavelength $\lambda \approx 128$ nm via excitation or ionization of argon atoms and their formation of excited Ar dimer states. Dimers produced via the excitation process emit a prompt component of the light with lifetime $\tau \approx 6$ ns. Those formed via ionization emit a slower component with $\tau \approx 1.6$ μs. The prompt component, representing about 25% of the light, proves more useful for triggering.

The interaction of charge particles and liquid argon produces light in the ultraviolet region [47]. The transitions from the two lowest molecular states ($^1\Sigma_u^+$ and $^3\Sigma_u^+$) to the ground state $^1\Sigma_g^+$ produces prompt and slow light. The potential curve [48] for an argon excited state is shown in Figure 4.3. These molecular states have two main origins. The first one is the direct excitation of excited states Ar^* by primary charged particles and secondary electrons. This excitation process is followed by the formation of molecular states, Ar_2^* with in 50 ns by a three-body collision process.

$$Ar^* + Ar + Ar \rightarrow Ar_2^*(^1\Sigma_u^+ or ^3\Sigma_u^+) + R \tag{4.1}$$

The second origin is the formation of two molecular states through a recombination process between thermalized electrons and molecular ions, Ar_2^*. The primary particles and secondary electrons produce atomic ions Ar^* and electrons. The atomic ions are converted to molecular ions Ar_2^* within 5 ns by the process:

$$Ar^+ + Ar + Ar \rightarrow Ar_2^* + Ar \tag{4.2}$$

The secondary electrons lose kinetic energy promptly through the excitation of excited states and/or production of electron-ion pairs and then through the elastic collisions, and they are finally thermalized. These thermalized electrons recombine with molecular ions forming highly excited atoms Ar^{**} via dissociative recombination:

$$Ar_2^+ + e \rightarrow Ar^{**} + Ar \tag{4.3}$$

The highly excited atoms relax via the reactions

$$Ar^{**} + Ar + Ar \rightarrow Ar_2^{**} + Ar \tag{4.4}$$

and

$$Ar_2^{**} + (Ar) \rightarrow Ar^{*} + Ar + (Ar) \tag{4.5}$$

and finally form excited molecules via reaction 4.2. All these process are outlined in Figure 4.2.

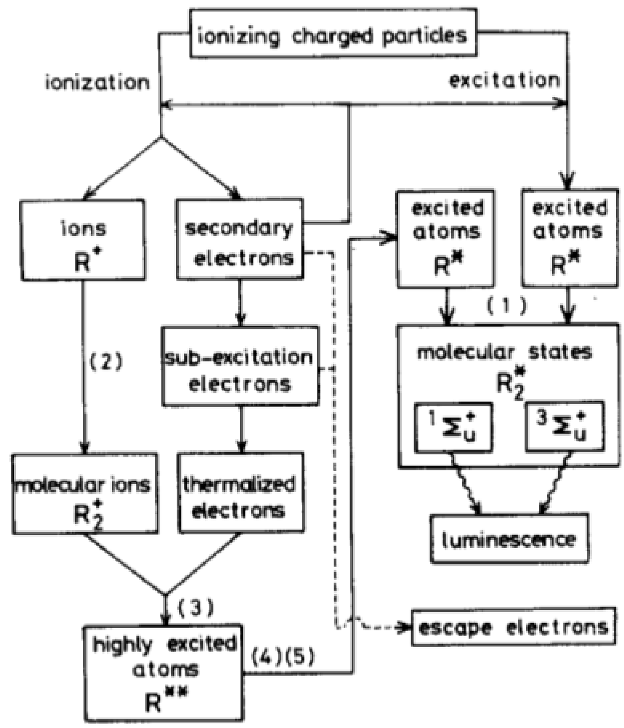

Figure 4.2: General reaction occurring in Argon when charged particle passes through it.

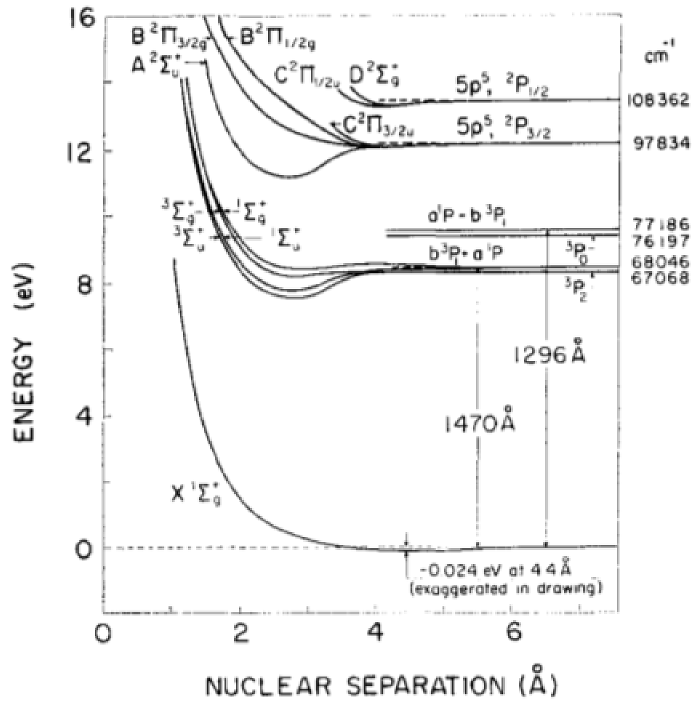

Figure 4.3: Potential curve for an argon excited state molecule [48].

Excimers are produced in two singlet states, ${}^1\Sigma_u^-$ and ${}^1\Sigma_u^+$ and in a triplet state ${}^3\Sigma_u^+$. The singlet state, ${}^1\Sigma_u^-$, does not emit photon because of the parity conservation. Therefore the scintillation light possesses two components: those stemmed from the transitions ${}^1\Sigma_u^+ \rightarrow {}^1\Sigma_g^+$(fast decay) and ${}^3\Sigma_u^+ \rightarrow {}^1\Sigma_g^+$(slow decay) where ${}^1\Sigma_g^+$ is the ground state. The decay of the singlet state is strongly allowed and its decay time, τ_1 is of the order of ns. The triplet state has a longer lifetime because of the strong spin-orbit coupling in Ar_2 and its decay time τ_2 is measured to be 1.6 μs. The scintillation emitted cannot be absorbed in LAr because the energy of photons is too low to excite the ground state atoms. The population of the singlet and triplet state depend on the ionization density.

4.3 Model for Reduced Scintillation Light at High Ionization Density.

A recoiling particle produces a track of excitons and ionized atoms which can be described in terms of core and penumbra as proposed by Hitachi and Doke [49]. The core is the zone of the track with a high energy deposition density and the penumbra surrounding the core corresponds to a lower density zone. Acoording to Hitachis model, the luminescence quenching occurs exclusively in the core via bi-excitonic collisions or penning processes apart from the fission fragment.

Assuming that the density of excitons and electron-ion pairs created along the track of the particle is directly proportional to electronic energy loss $(\frac{dE}{dx})_{elec}$, the scintillation light yield can be written without taking into account the luminescence quenching as

$$\frac{dS}{dx} = A\left(\frac{dE}{dx}\right)_{elec} \tag{4.6}$$

Where A is a proportionality constant. There is also a proportionality between the local concentration of the core and the electronic stopping power which is given by $B\left(\frac{dE}{dx}\right)_{elec}$. To take into account the probability of the quenching, the overall collision probability in the core, which is denoted by k, must be implemented in the Eq. 4.6. In the process of the luminescence quenching, the scintillation light response is described by the Birk's law saturation:

$$\frac{dS}{dx} = \frac{A\left(\frac{dE}{dx}\right)_{elec}}{1 + kB\left(\frac{dE}{dx}\right)_{elec}} \tag{4.7}$$

and therefore the reduced scintillation light at high ionization density can be expressed as

$$f_l = \frac{1}{1 + kB\left(\frac{dE}{dx}\right)_{elec}} \tag{4.8}$$

For LAr, $kB = 7.4 \times 10^{-4} MeV^{-1} gcm^{-2}$ was determined from heavy ion measurements assuming a quenching factor of 46%.

4.4 The Effect of Impurities

Impurities in LAr (N_2,O_2,H_2O and $CO + CO_2$), caused by the outgassing in the detector can quench argon excimers or absorb the ultra-violet scintillation light emitted from the argon excimer decay. The expected effect of the non-radiative collisional reaction represented in Equation 4.9, is a decreased the triplet lifetime, observed by Himi et al. [50] by increasing the concentration of N_2 during the measurement. Since triplet states have a long lifetime, they undergo various collisions with neighbors before decaying eventually, which leads to a reduction of the scintillation light intensity.

$$Ar_2^* + X \rightarrow 2Ar + X + KE \tag{4.9}$$

Where X is nucleaus and KE is kinetic energy.The WArP collaboration has recently carried out additional studies to quantify the reduction of the triplet lifetime and the quenching of the scintillation light in LAr caused by N_2 and O_2 contaminants [51]. The triplet state is the scintillation component that is the most affected by the contamination.

4.5 PMTs in mini-CAPTAIN

By detecting the scintillation light produced during interactions in the CAPTAIN detector, the photon detection system provides valuable information. The amount of light produced by a particle traversing argon is a function of the energy deposited. The scintillation light can be used to determine the energy of neutrons from time of flight when the experiment is placed in a neutron beam line by giving the time of the interaction with resolution of a few nanoseconds.

Liquid argon scintillates at a wavelength of 128 nm which unfortunately is readily absorbed by most photo detector window materials. It is necessary to shift the light to the visible. The photon detection system is composed of a wavelength shifter covering a large area of the detector and a number of photo detectors to collect the visible light. The baseline mini-CAPTAIN photon detection system uses tetraphenyl butadiene (TPB) as a wavelength shifter and sixteen Hamamatsu R8520-500 photomultiplier tubes (PMT) for light detection. The R8520 is a compact PMT approximately 1 x 1 x 1 in size with a borosilicate glass window and a special bialkali photocathode capable of operation at liquid argon temperatures (87 K). It has a 25 % quantum efficiency at 340 nm. TPB is the most commonly used wavelength shifter for liquid argon detectors and has a conversion efficiency of about 120% when evaporated in a thin film. It has a re-emission spectrum that peaks at about 420 nm [52]. The TPB will be coated on a thin piece of acrylic in front of the PMTs. All sixteen PMTS are located on the bottom of the TPC. This system will provide a minimum detection of 2.2 photoelectrons per MeV for a MIP.

The PMTs use a base with cryogenically compatible discrete components. The cable from the base to the cryostat feedthrough is a Gore CXN 3598 with a 0.045 diameter to reduce the overall heat load. The PMT signals are digitized at 250 MHz using two 8-channel CAEN V1720 boards. The digitizers are readout through fiber optic cables by a data acquisition system written for the Mini-CLEAN experiment [53]. The sixteen PMT configuration is show in Figure 4.4. The PMT array is fixed behind the TPC cathode plane. A copper plate is used to shield them from the electric field. A copper grid and TPB coated window is situated in front of each tube. Holes were made in the copper plate to allow liquid argon to flow through the fiducial volume.

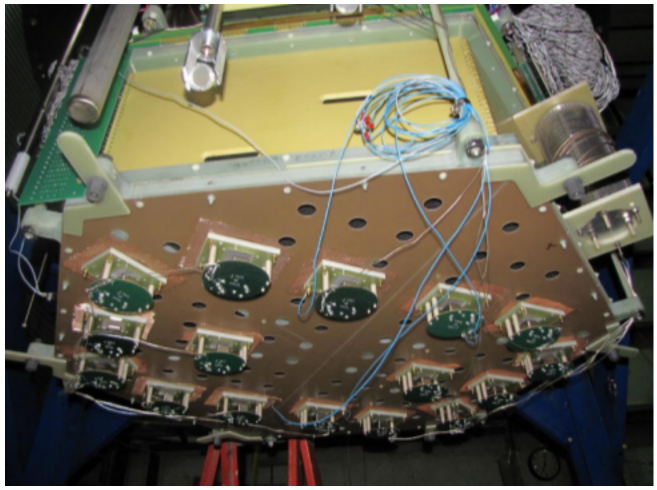

Figure 4.4: PMTs installed at the bottom of the TPC.

4.6 Wavelength Shifter

The $\lambda \approx 128$ nm scintillation light in LAr must be shifted to the visible in order to be detected by the photo tubes. A tetraphenyl butadiene (TPB) layer acting as a wavelength shifter performs this task in mini-CAPTAIN. The absorption and emission spectra are shown in Figure 4.5. The TPB absorbs in the UV and emits in the visible with a peak emission at $\lambda \approx 425 \pm 20$ nm, a favourable wavelength for detection by PMTs. The WLS emits an average of 1.2 visible photons for every 128 nm photon absorbed

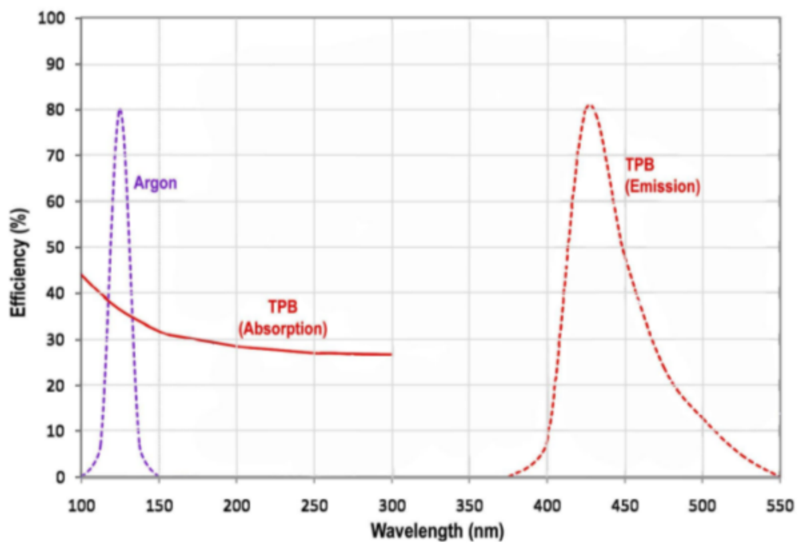

Figure 4.5: TPB layer emission and absorption spectra in the high UV.

Chapter 5

Measuring Neutron Interactions in a Liquid Argon TPC

5.1 Neutron Interaction in Liquid Argon

The type of neutron interactions with an argon atom depends on the energy of the incident neutron. Neutrons being neutral particles, they do not interact directly with electrons but are confined to direct nuclear effects and nuclear reactions. The three types of interaction that neutrons may undergo in LAr are the following:

- Elastic scattering producing nuclear recoils
- Inelastic collision leading to γ emission and nuclear recoils
- Neutron capture with subsequent emssion of a γ and Auger electrons

For fast neutrons (neutrons with an energy greater than 1 MeV), elastic collisions is the most important interaction process to produce nuclear recoils. The energy, E_R, transferred by the projectile particle into a target nucleus with an atomic mass A can be generalized as [54]

$$E_R = \frac{2m_n E_n}{(m_n + A)^2}\left(m_n + A - m_n cos^2\theta - \cos\theta\sqrt{A^2 + m_n^2 cos^2\theta - m_n^2}\right), \tag{5.1}$$

where m_n is the mass of the projectile, E_n its energy and θ the scattering angle in the laboratory frame. In the case of non relativistic neutrons ($E_n << m_n c^2$) interacting with a heavy target such as argon ($A >> m_n$), the Eq. 5.1 can be approximated as

$$E_R \approx \frac{2A}{(1+A)^2}\left(1 - cos\theta\right) E_n \tag{5.2}$$

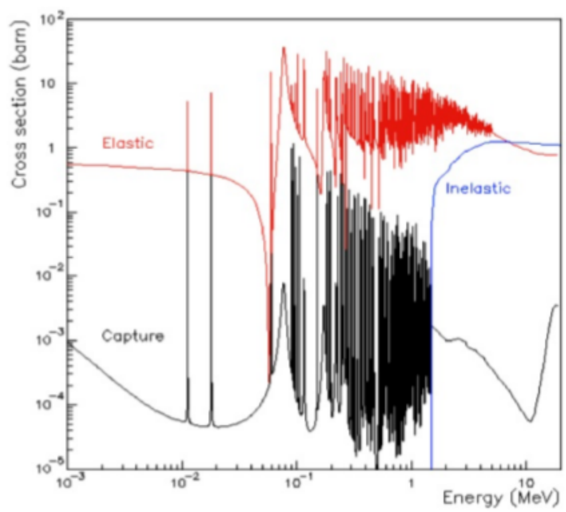

Figure 5.1: Neutron elastic scattering (red), inelastic scattering (blue), and capture (black) cross sections on LAr([55].

Beyond a couple of MeV energies, the effect of the inelastic collision is not negligible, being approximately 1 order of magnitude lower than the elastic collision for an incoming neutron at 2.45 MeV. Inelastic scatterings produce low energy γ ($\approx$keV) and Auger electron of energy $\approx 9.4\ eV$. The neutron capture reaction should dominate for thermal energies (0.025 eV) and resonances are also observed in the keV energy range. The $^{40}Ar(n,\gamma)^{41}Ar$ reaction produces a keV electron and a 1.3 MeV γ from the ^{41}Ar decay. Figure 5.1 shows the cross-section for neutron total elastic scattering, inelastic scattering and neutron capture in LAr as as function of the energy.

5.2 Simulation Studies

The simulation of the neutron propagation and its interaction was done by GEometry ANd Tracking (Geant4) package [56]. Although Geant4 accurately describe the particle propagation in the medium and its interaction, it is lacking in terms of light simulation in liquid argon. Several groups are trying to make a new simulation package to simulate light in liquid argon. Reactor Analysis Tool (RAT) [57] is one example. RAT is a simulation and analysis package built with GEANT4, ROOT, and C++, originally developed by S. Seibert for the Braidwood Collaboration. Versions of RAT are now being used and developed by several particle physics experiments.

The purpose of simulation studies is to validate the software. Ten thousand neutrons are generated at (-2320,0,0) cm where the neutron beam is located. The (0,0,0) is the center of the mini-CAPTAIN. All neutrons travel toward the detector, negative x to positive x. The energy of those neutrons linearly increases from 0 - 800 MeV. The starting positions of neutrons are shown in Figure 5.2.

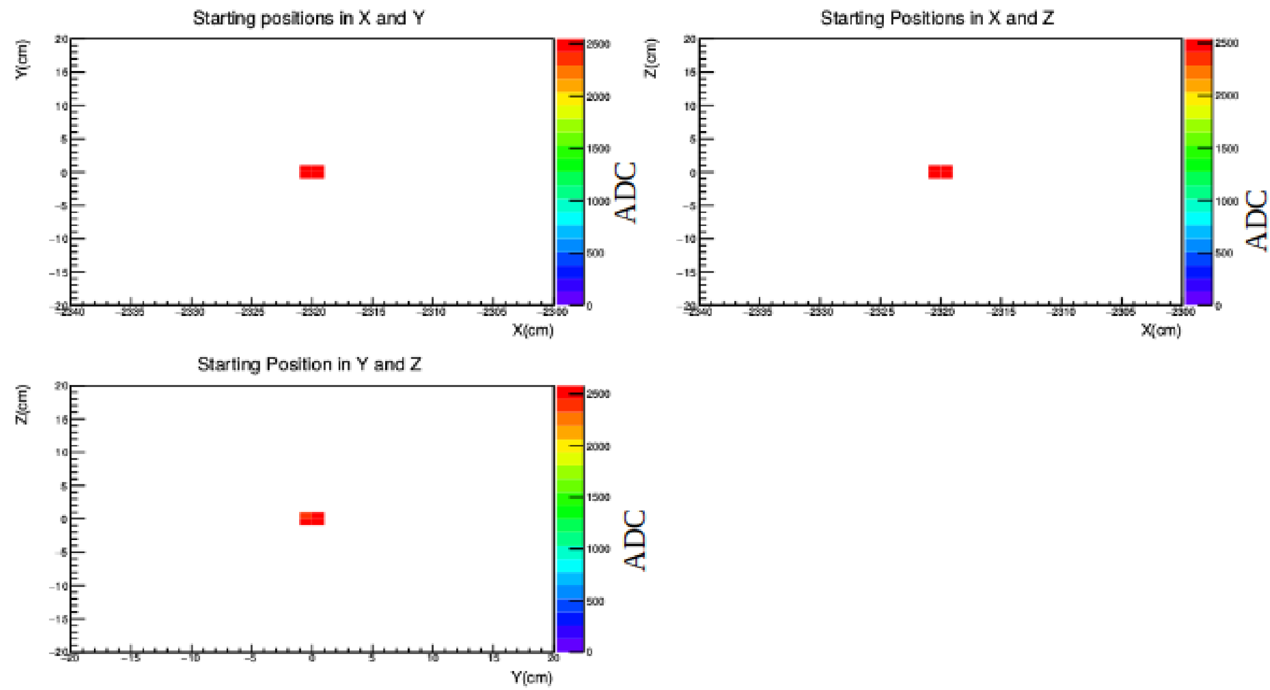

Figure 5.2: Starting point of simulated neutrons in 2D. Color in the column represent the charge in analog to digital (adc) count.

The momentum of neutrons is shown in Figure 5.3. We have momentum only along x axis since all neutrons are traveling toward the positive x axis.

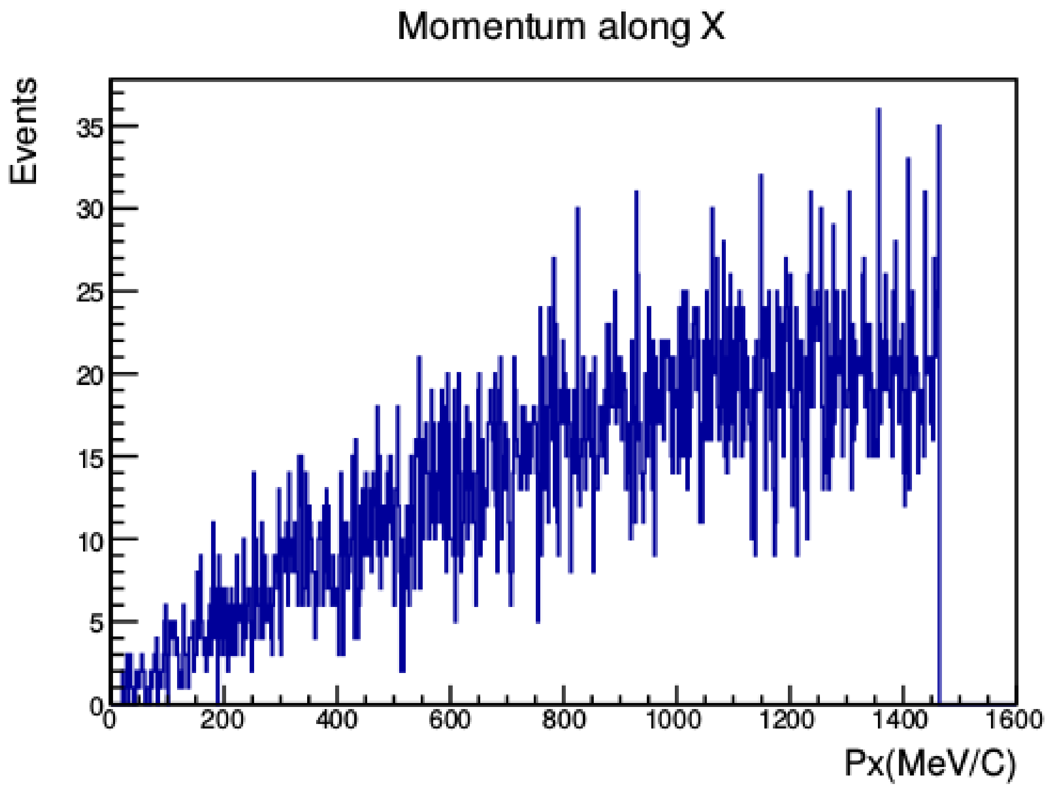

Figure 5.3: Momentum of simulated neutrons in starting position

We also wanted to know the neutron interaction point inside the detector. Figure 5.4 shows the interaction points inside the fiducial volume (apothem 45 cm and drift 30 cm). There are a lot of interactions of neutrons with the cryostat, not shown in the figure because the cryostat is outside of the fiducial volume.

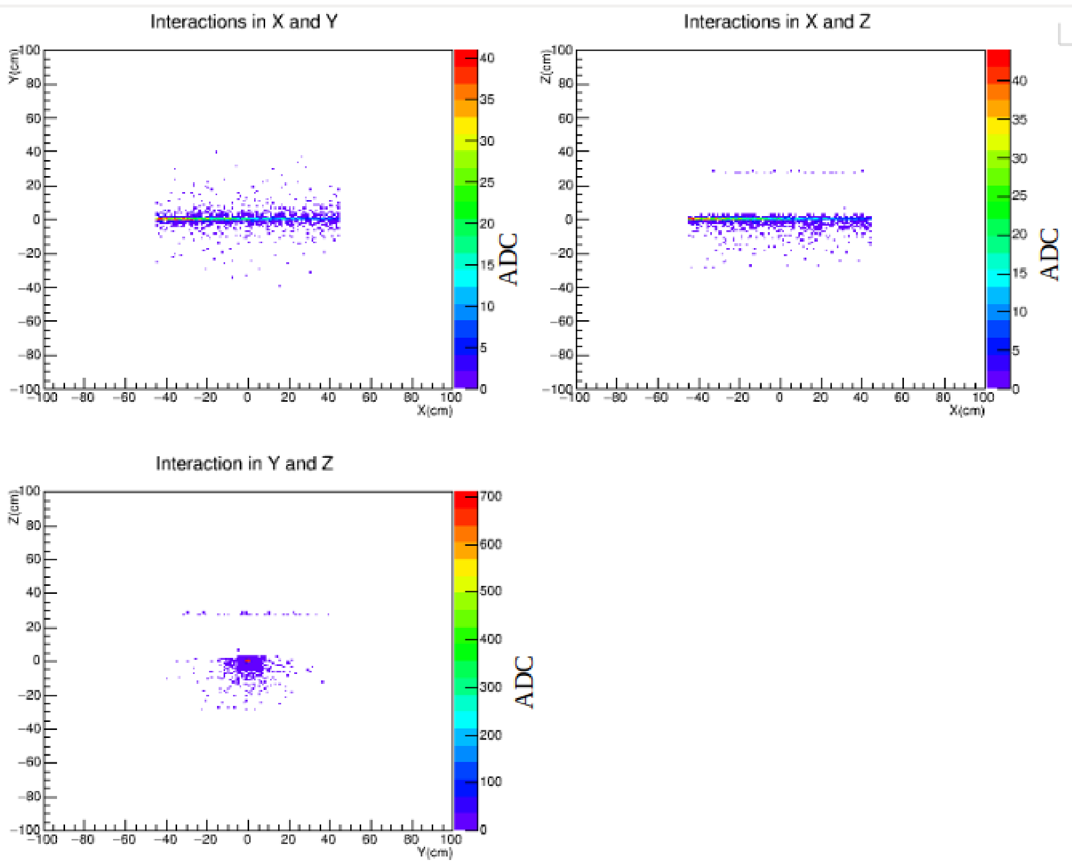

Figure 5.4: Simulated interaction points inside the fiducial volume in 2D. Top left: Interaction in X and Y, looking down on the detector from above. Top right: Interaction in X and Z, looking at the detector from the side. Bottom left: Interaction in Y and Z, looking along the beam direction. Color in the column represent the charge in ADC.

I also plotted the PMTs hit position in X and Y. Figure 5.5 shows the PMTs hits in X and Y. It clearly shows the PMT position in the detector and it exactly matches with the physical location of the PMTs.

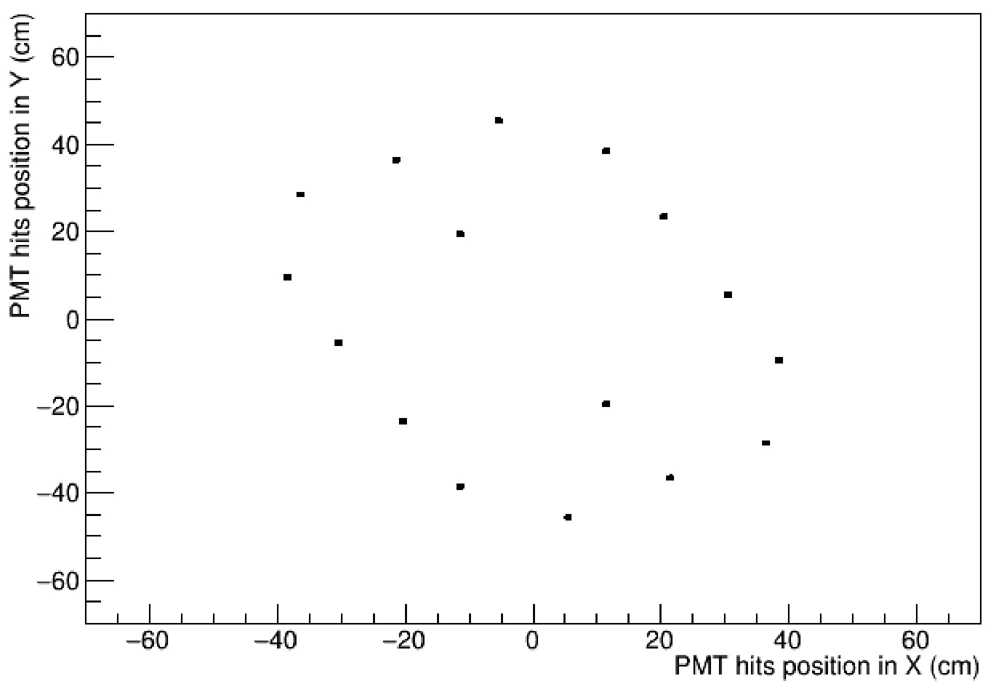

Figure 5.5: Simulated PMTs hits in the X and Y (cm) directions. We can see the sixteen PMTS and their location match with the physical location of the PMTs.

From the simulation, we know the time at the generation point and the time of interaction. I subtracted two times to get the time of flight of the simulated neutron. Figure 5.6 shows the time of flight of simulated neutrons in nanoseconds.

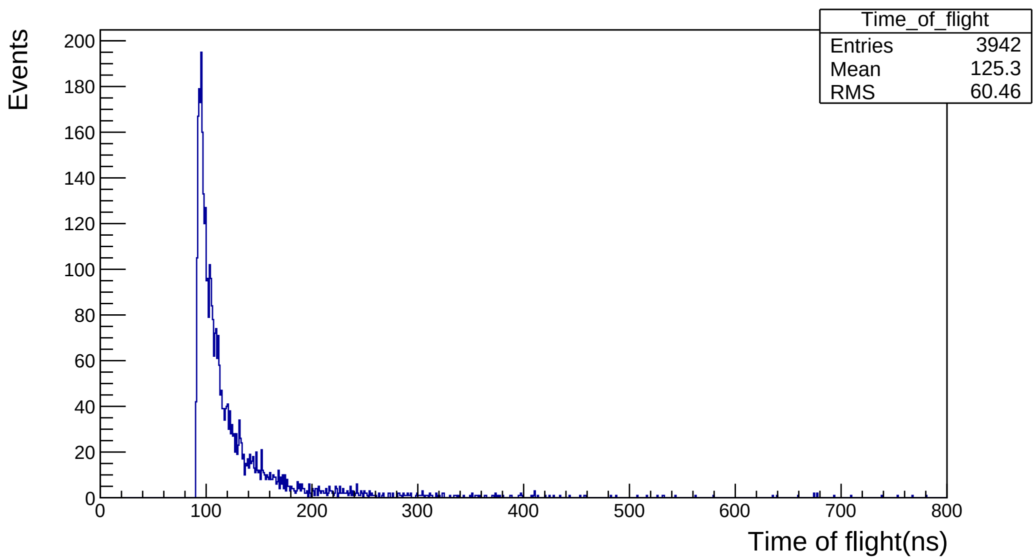

Figure 5.6: Time-of-flight of simulated neutrons whose primary vertex is inside the fiducial volume.

We changed the time of flight to energy using the relativistic relation 6.3, which is shown in Figure 5.7.

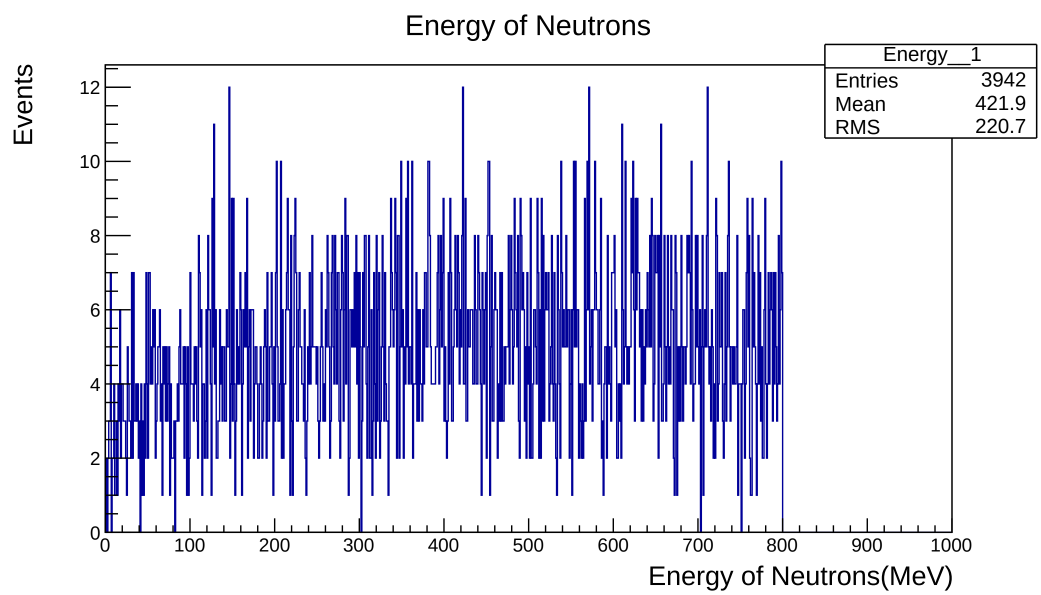

Figure 5.7: Kinetic energy of simulated neutrons whose primary vertex is inside the fiducial volume.

5.3 Neutron Beam Generation at Los Alamos National Laboratory

The Weapon Neutron Research facility uses a proton beam that is chopped and bunched to generate an adjustable pulse-to-pulse separation, typically 1.8 μs [58]. The beam strikes a tungsten target producing neutrons, gamma rays and charged particles. The charged particles are removed from the beam by permanent magnets. Neutrons (with gamma rays) are collimated to form beams for six flight paths viewing the neutron source at angles to the left (L) or right (R) relative to the incident beam direction of 15°,30°,60°, and 90° as shown in Figure 5.8. The neutrons and gamma rays travel the distance of the flight path to arrive at a sample or detector. Because gamma rays travel at the speed of light, the gamma rays arrive first. As the neutrons traverse the flight path, the neutron pulse becomes broader with the highest energy neutrons arriving before the lower energy neutrons. A measurement of the time between the beam pulse and the detection of a signal from the detector gives the energy of the neutron [58].

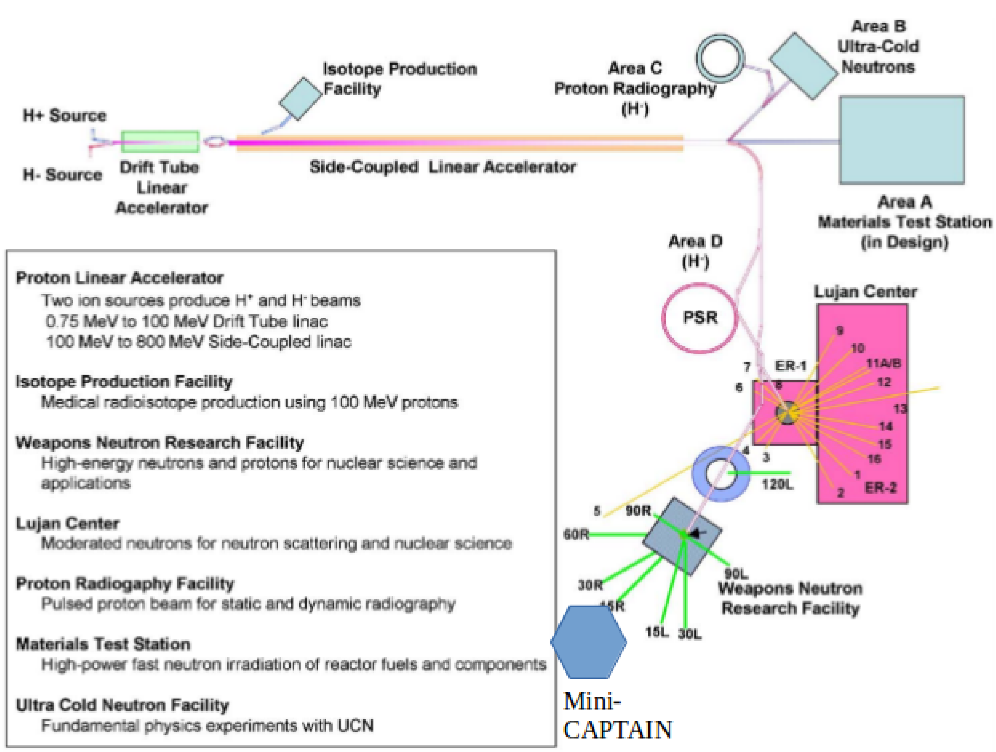

Figure 5.8: Layout of the LANSCE user facility. mini-CAPTAIN was placed at the flight path 15R in WNR.

5.4 mini-CAPTAIN Neutron Run

The neutron measurement with mini-CAPTAIN was taken at the WNR facility on the LANSCE accelerator. It is located at Los Alamos National Laboratory (LANL). Figure 5.10 shows the setup of mini-CAPTAIN in flight path 15R. The recirculation, electronic racks, and computers were situated along the wall outside the beam path. Due to the long purification time for mini-CAPTAIN, it was initially filled and purified outside of the enclosure. The initial liquid argon quality was 2.7 ppm for oxygen and 0.5 ppm for water. We purified the liquid argon by recirculating. It took us a month to reach 1 ppb from several hundred ppb. The relation between the number of days and purity is shown in Figure 5.9. A few days before our neutron run, two of the shielding blocks were moved and mini-CAPTAIN was rolled into position. All of the electronic cables and the cryogenic plumbing had to be removed during the cryostats transition.

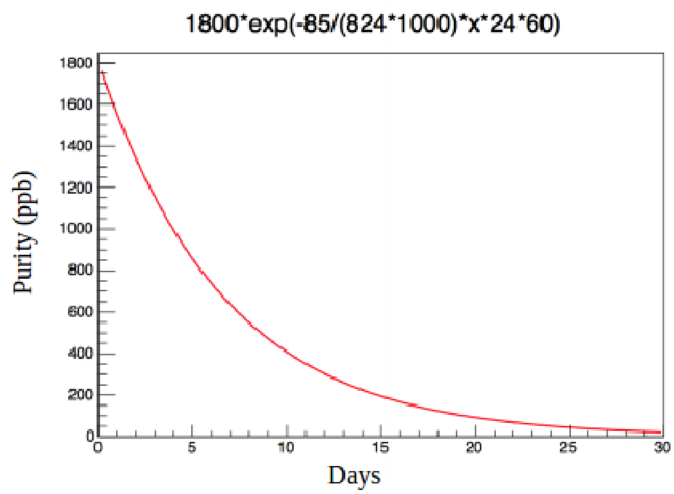

Figure 5.9: Purity change by the number of days for initial purity of 1800 ppb. X axis is number of days and Y axis is purity in ppb. Figure by Qiuguang Liu.

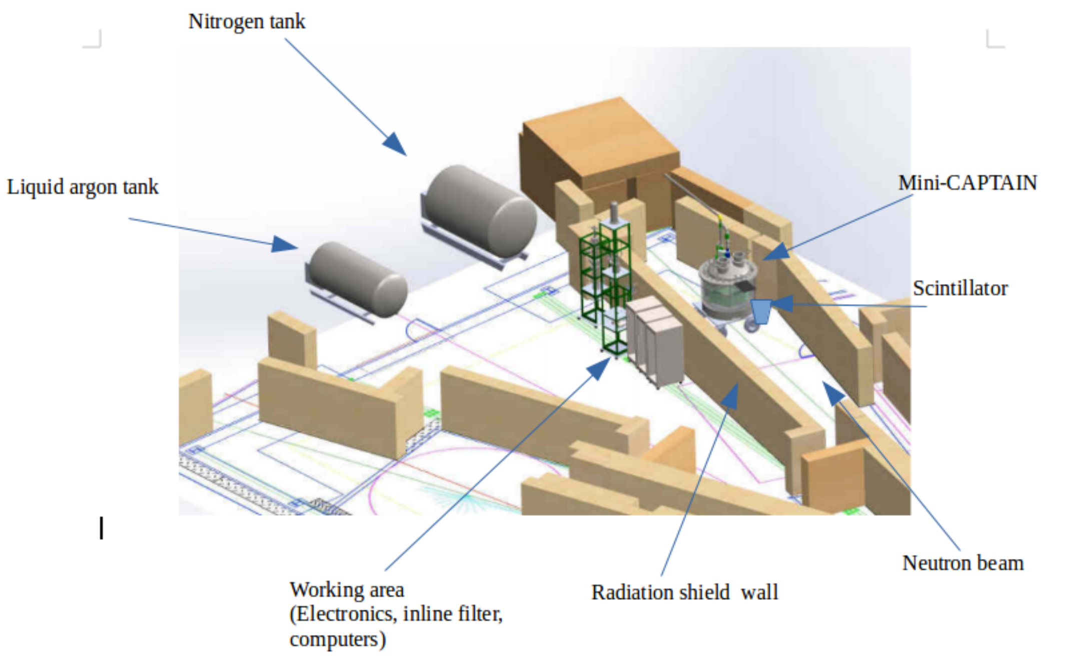

Figure 5.10: The mini-CAPTAIN neutron run was taken in the 15R flight path at the WNR facility on the LANSCE accelerator

The neutron running was broken into two phases: high intensity and low intensity runs. For the high intensity run, the beam was delivered at its usual rate of 3.8 μA. The shutter to flight path 15R was partially closed to reduce the rate at which neutrons would enter mini-CAPTAIN. The first couple hundred runs, showed a high neutron rate from the data acquisition (DAQ) output. The shutter opening was further reduced to a rate of less than one neutron per second. On the last day of data collection, the accelerator team delivered a 1 Hz beam for our scheduled low intensity run.

5.5 Trigger Setup

The beam, as shown in Figure 5.11, was delivered in large bunches (macropulse) of smaller pulses (micropulse). The macropulses were 625 μs long and separated by approximately 8.3 ms, which corresponds to a repetition rate of ≈120 Hz. The smaller micropulses were typically 1.8 μs apart, but for our run, the micropulse separation was set to low-intensity around 200 μs. The TPC was forced to trigger on the first micropulse in a macropulse. After each trigger, the TPC trigger is vetoed for half a second up to two seconds (depending on the runs predetermined DAQ trigger rate). Figure 5.11 illustrates the timing between the beam RF signal, PDS activity, PDS trigger and TPC acquisition gate as seen on the oscilloscope.

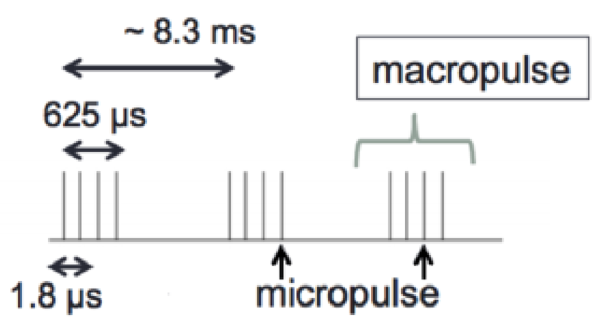

Figure 5.11: The beam is delivered in bunches of 625 micropulses every 8.3 ms. The micropulses are typically separated by 1.8 μs. For our low-intensity run, the micropulse separation was ≈200 μs.

The overall triggering scheme is shown in figure 5.12. The accelerator's RF signal opens a 100 ms gate generator and triggers the TPC DAQ. Its signal is recorded on channel 5 on each of the PDS digitizers. Once the 100 ms gate is open, the trigger is sent to a 4 ms gate. The analogue fan-in-out then takes the integrated charge from the individual PMT counters and passes them to the discriminator. If the summed value exceeds the threshold, the trigger is passed to the PDS boards and GPS for recording.

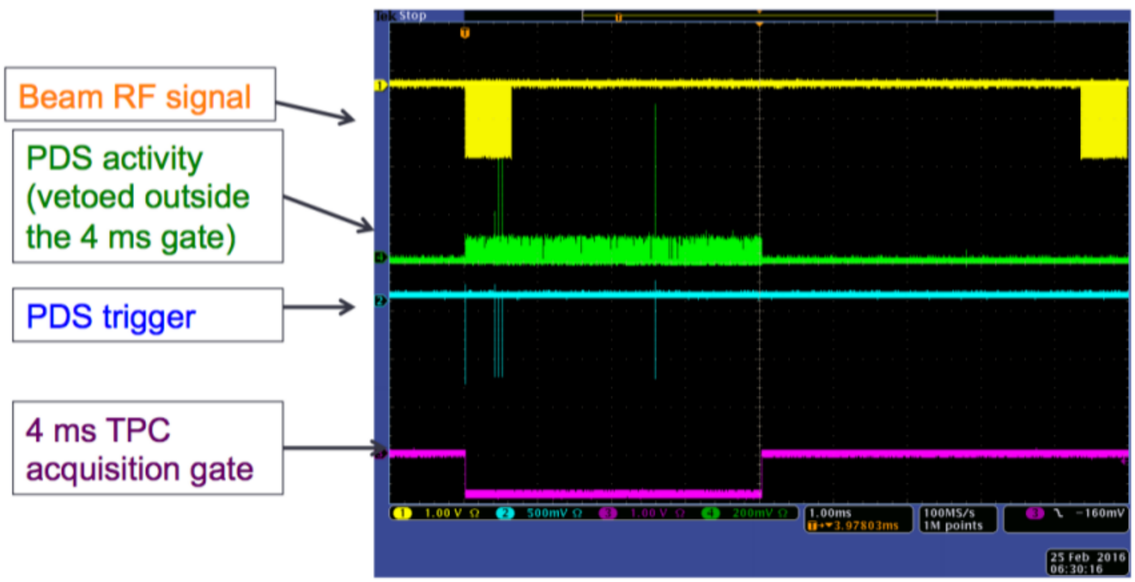

Figure 5.12: The trace of the beam RF signal, PDS activity, PDS trigger and TPC acquisition gate as seen on the oscilloscope.

Chapter 6

Data Analysis

6.1 Scintillator Data Analysis

We took data with mini-CAPTAIN in the neutron beam at Los Alamos in February 2016 for one week. We ran the mini-CAPTAIN with two beam configurations, high-intensity and low-intensity. In the low-intensity mode, we expected one neutron per macro pulse. For the studies presented in this thesis, we only used the low-intensity data.

We have twenty low-intensity runs but two of them did not have any scintillator pulses. So we used 18 runs for analysis. We used data from the scintillator and photon detection system (PDS) for the analysis. The size of scintillator data is 400 GB. Data was stored in a ROOT file in PDSF, NERSC computing center. The scintillator recorded the voltage each nanosecond for 650 microseconds. Therefore for each event, there is an array with 650,000 voltage readings.

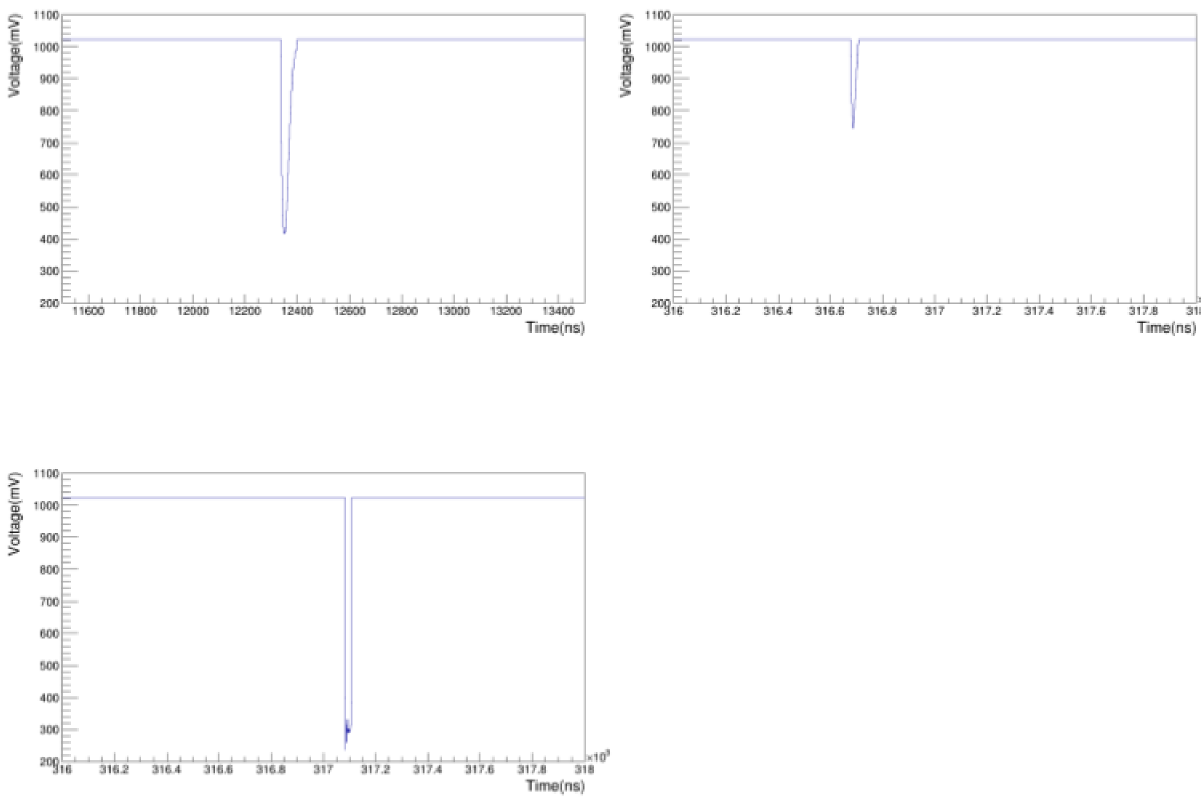

Figure 6.1: Typical neutron (top left), gamma (top right) and RF (bottom left) waveform. X axis is the time in ns and Y is the voltage in mV. The repetition rate for RF is 196 μs.

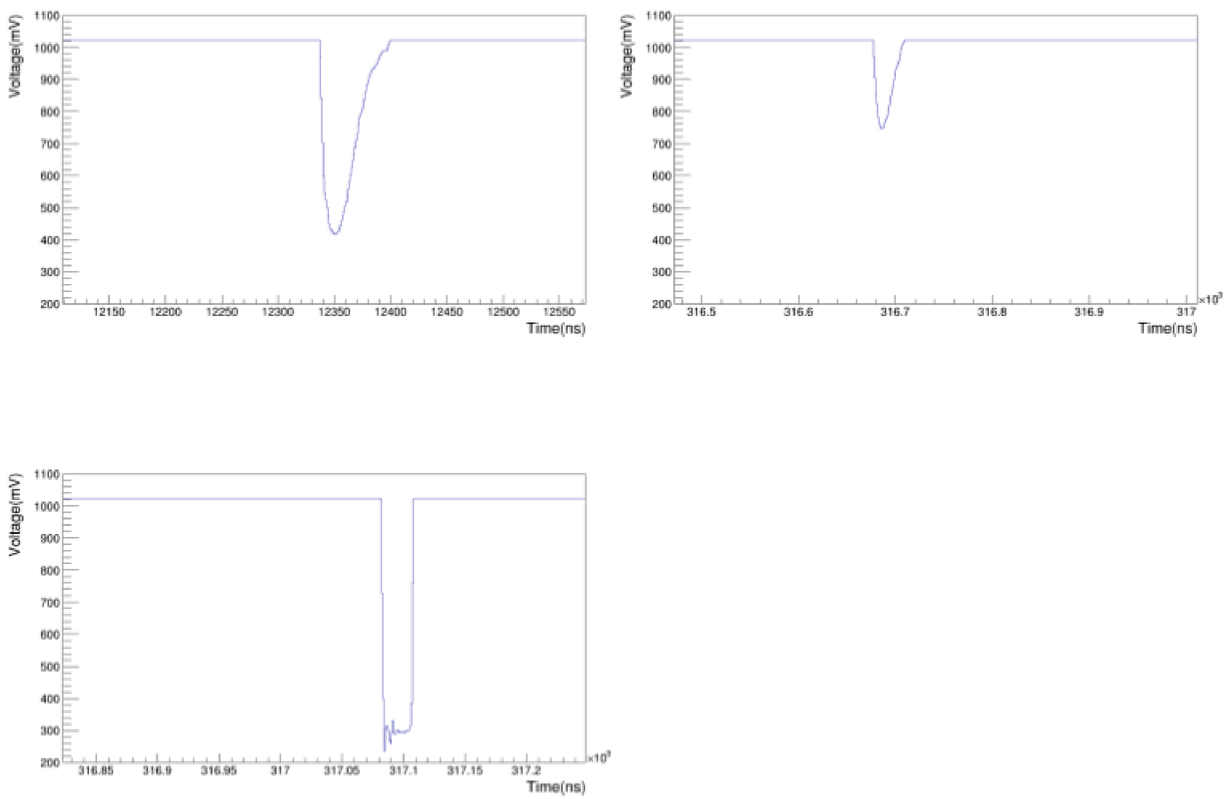

Figure 6.2: Zoomed in version of the plot 6.1

.

6.1.1 Scintillator Analysis Code

Scintillator data were stored in a ROOT file as shown in Figure 6.3. The data acquisition system (DAQ) system that we used to acquire the data had 4 input channels. The scintillator pulse was recorded on channel 0. The scintillator signal was also discriminated by a NIM threshold discriminator module and the output of the discriminator was recorded on channel 2. The beam trigger (RF) pulse was acquired on channel 3. The trigger was a square signal occurring at the beginning of a 625 μs beam gate. The sampling rate was 1 GHz, i.e., one sample/ns, and the data acquisition window was slightly longer than the 625 μs beam gate.

Each file contained a ROOT tree named event_tree. The variables that we have to look inside the tree are **ev_samples** and **ev_channel**. The variable ev_channel tells us which input signal we are looking at (channel 0 3), ev_samples contains the voltage samples relative to one data acquisition window (about 640 μs long). For every event, ev_samples contained an array with 650,000 entries, since we were sampling the voltage at 1 GHz for 650 μs each time. The other variables were not filled at this stage.

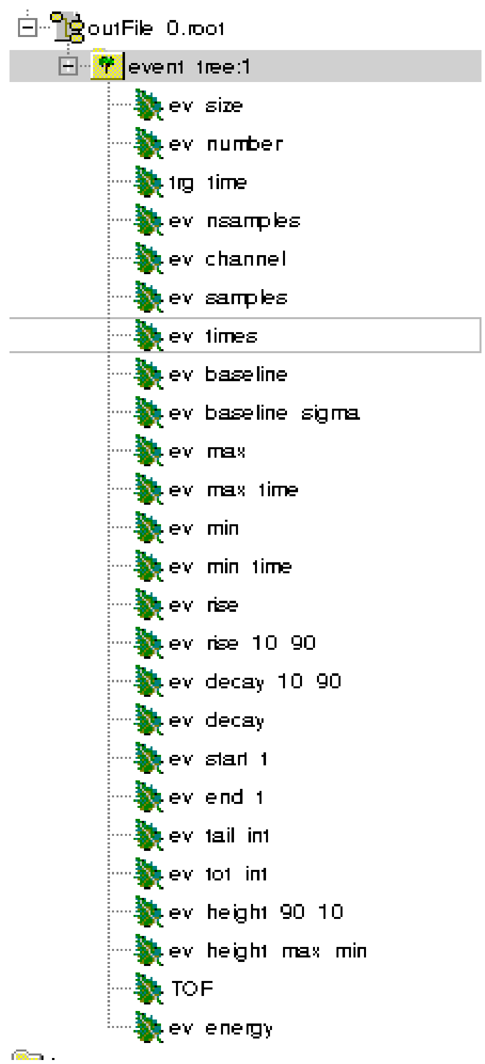

Figure 6.3: Scintillator data format

The method I used to find the time of flight from the scintillator is as follows. First, I plotted the ev_samples entries vs time for 625 μs for each event, which showed the scintillator waveform. The pedestal value was 1023 mV. For each waveform, I found the time for which the voltage was less than or equal to 1010 mV. This is the time of the leading edge of the pulse, and I defined this as the pulse time. For each scintillator pulse (channel 0), I subtracted the pulse time from the closest RF pulse time (channel 3). The closest is used because the RF pulse comes for each micropulse, approximately every 200 μs, which is much greater than the time of flight even for low energy neutrons. For example, the time of flight for a 1 MeV neutron in our beam line is less than 2 μs. Typical neutron, gamma, and RF pulses are shown in Figure 6.1. Their enlarge version is shown in Figure 6.2. The width of the waveform from a gamma and from a neutron is $\approx$10 ns and $\approx$130 ns, respectively, which also can be seen from these waveforms.

6.1.2 Neutron Energy Spectrum from Scintillator Data

The time of flight distribution is shown in Figure 6.4. This is the time of flight from the production point (beam target) to the scintillator. As we can see, there is a peak near 70 ns which is due to gamma rays. We removed the gamma peak by fitting a Gaussian and subtracting the fitted Gaussian from the time of flight. The fitted and enlarged fitted plots are shown in Figures 6.5 and 6.6, respectively. As we can see from the enlarged plot, the fitting was not perfect. There was still background due to gamma rays left in the time of flight plot. Future analyses can further remove this background using pulse shape discrimination between neutron and gamma ray pulses.

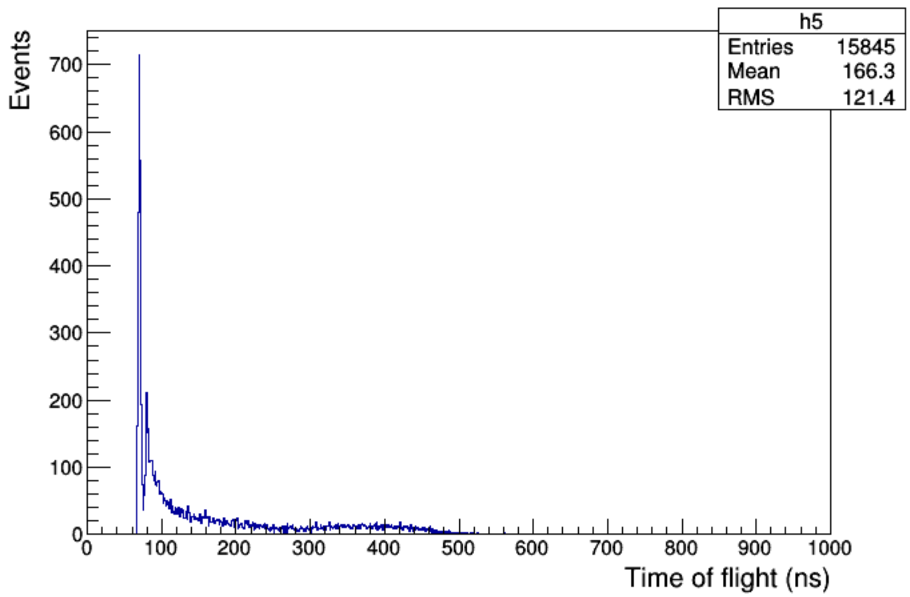

Figure 6.4: Time of flight distribution from the scintillator data analysis. The peak near 70 ns is due to gamma rays.

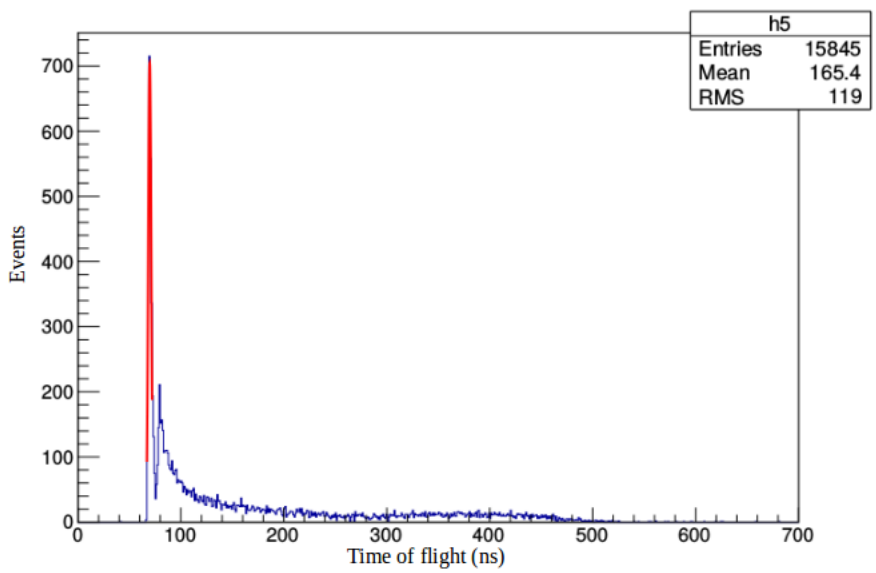

Figure 6.5: Gamma peak fitted with Gaussian. The purpose is to remove gammas from the neutron time of flight spectrum.

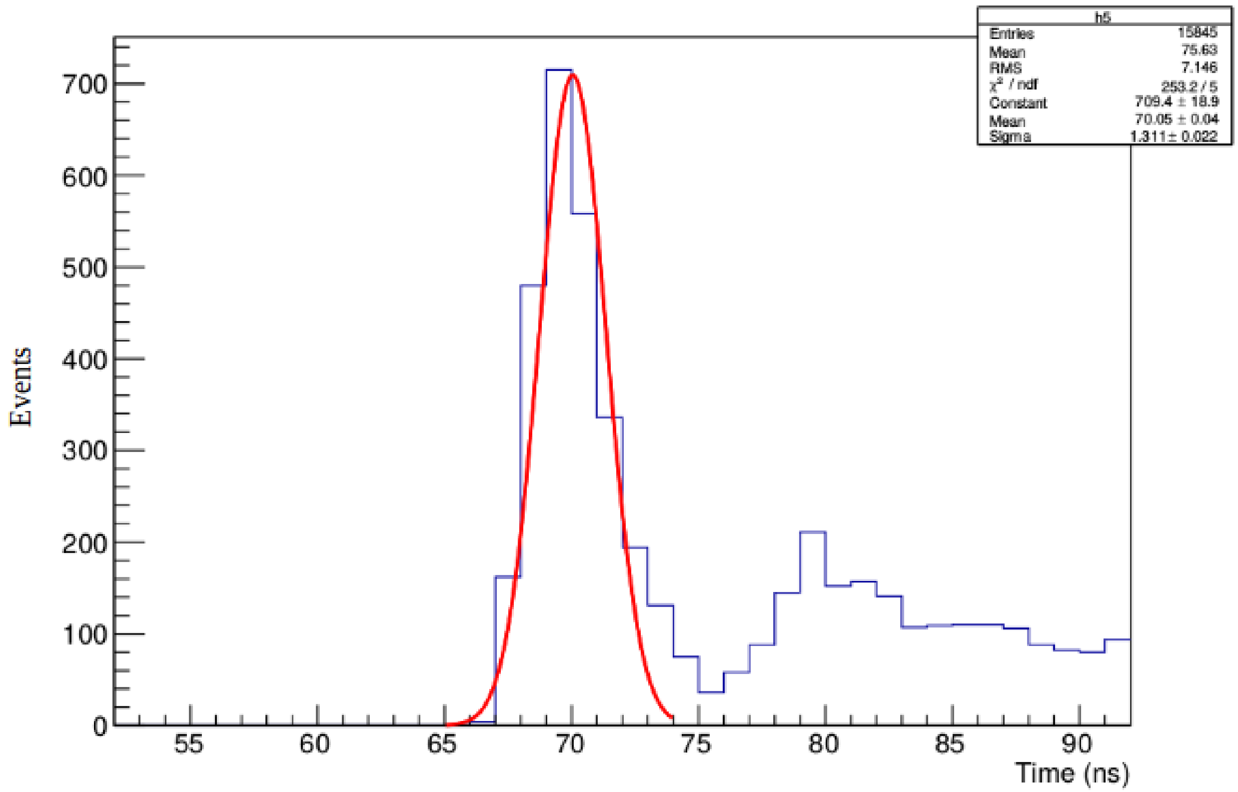

Figure 6.6: Enlarged gamma peak from Figure 6.5.

The time of flight plot after gamma subtraction is shown in Figure 6.7. A broad peak can be seen around 350 ns. We suspect this background is due to neutrons reflecting back from the mini-CAPTAIN cryostat into the scintillator. A time of flight of 350 ns corresponds to an energy of 19.4 MeV. To remove this background, I fitted an exponential to the time of flight spectrum in the region 100 - 250 ns, shown in Figure 6.8. Neutrons in excess of what was predicted by the exponential function for time of flight greater than 250 ns were considered background. Figure 6.9 shows the time of flight distribution with the background subtracted.

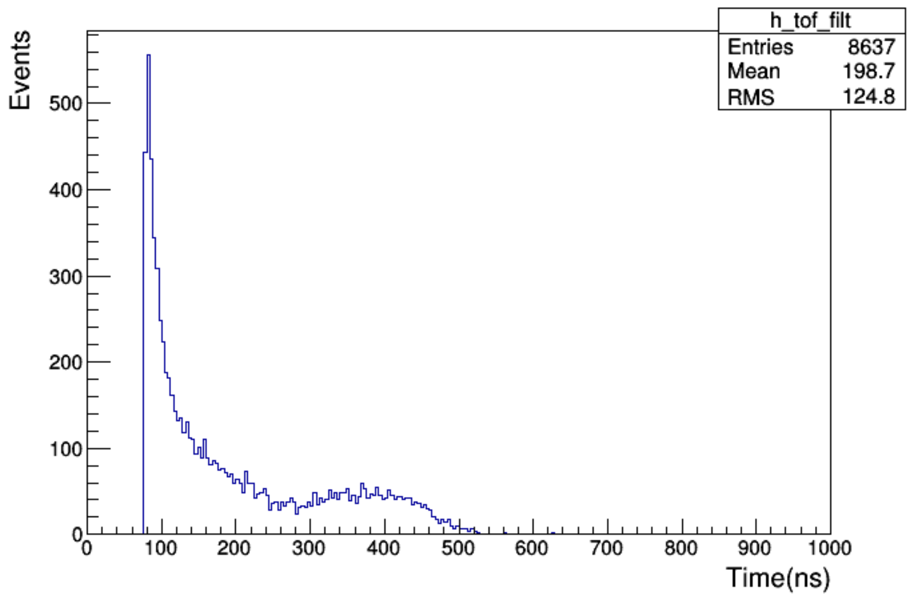

Figure 6.7: Time of flight of neutrons from their production point to the scintillator.

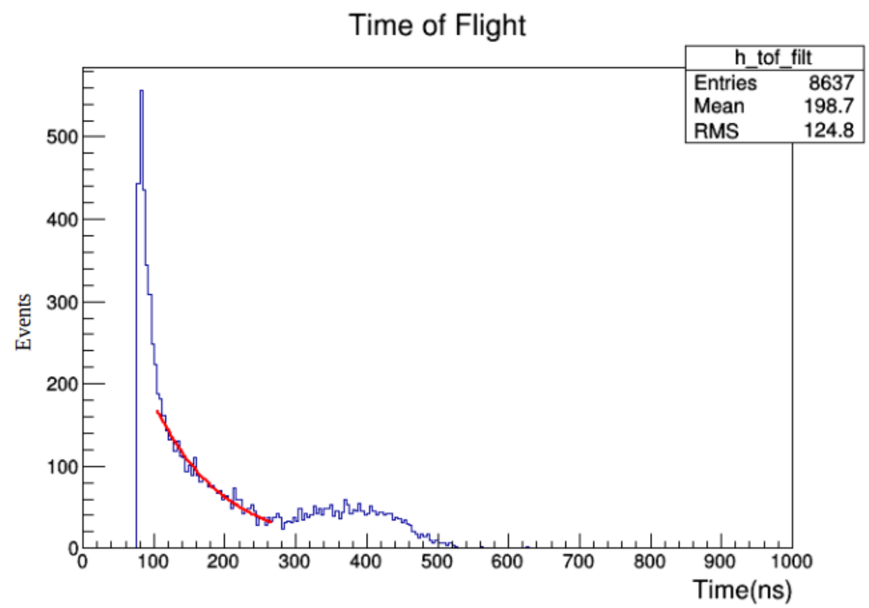

Figure 6.8: Exponential fitting to remove the broad peak near 350 ns due to likely background.

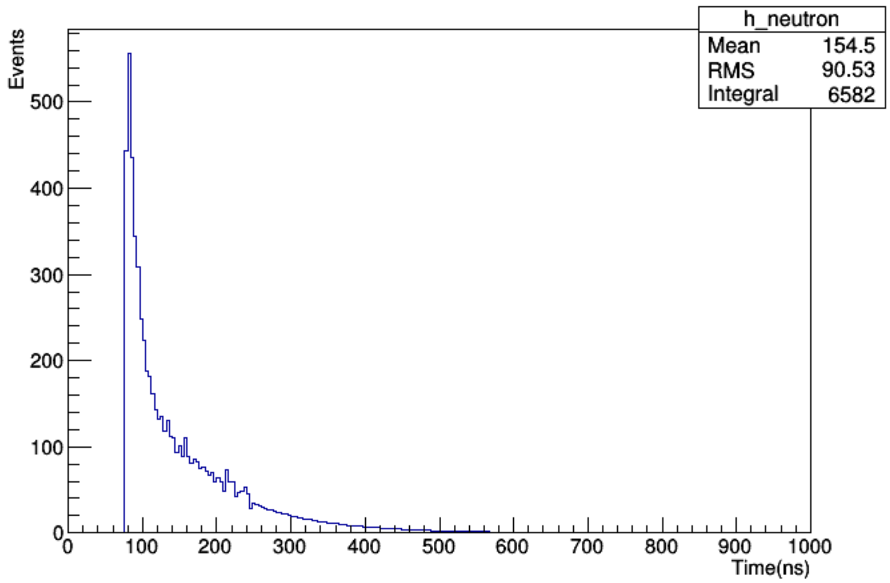

Figure 6.9: Time of flight of neutrons from their production point to the scintillator

The distance from the production point (the beam target) to the scintillator was 20 m. The time of flight is converted to energy using the following relativistic equations.

$$p = \frac{Lm}{\sqrt{(tc)^2 - L^2}} \tag{6.1}$$

$$E_{kin} = \sqrt{p^2 - m^2} - m \tag{6.2}$$

Combining Equations 6.1 and 6.2 with the correct units gives:

$$E_{kin} = m_o \left[\frac{1}{\sqrt{1 - (3.3356 * L/t)^2}} - 1 \right] \tag{6.3}$$

where E_{kin} is the kinetic energy of neutron in MeV, m_0 is the rest mass of the neutron in MeV, L is the length in meters, and t is the time in nanoseconds.

The kinetic energy based on time of flight is shown in Figure 6.10. This is an independent energy measurement of neutrons that go to TPC. The small peak near 900 MeV is probably due to leftover gamma rays.

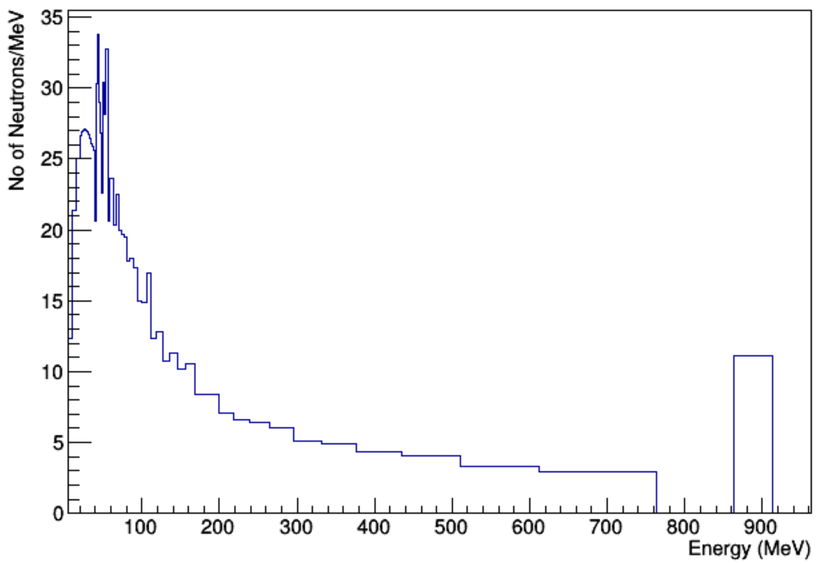

Figure 6.10: Normalized neutron energy from scintillator data in MeV. The peak near 900 MeV is likely due to background gamma rays. The Y-axis is number of neutrons per MeV. Each bin corresponds to 4 ns time of flight. The peaks around 50 MeV are due to imperfect removal of the background.

6.1.3 Future Work

The purpose of placing the scintillator upstream of mini-CAPTAIN was to measure the absolute neutron flux. However, the data to evaluate the neutron detection efficiency in scintillator was not available. The method developed in this analysis to determine the neutron energy spectrum in the scintillator will be used with efficiency data in the future to determine the neutron flux.

6.2 Photon Detection System (PDS) Data Analysis

During the neutron run, 15 of the 16 PMTs installed in mini-CAPTAIN were supplied with HV and read out through the digitizer. Further analysis after the neutron run showed that one PMT was not functional during the run, so 14 of the 16 PMTs provided useable data during the run. The PMTs were read out with three digitizers: each digitizer output 5 channels of PMT data and a 6th channel recorded the accelerator RF pulse. The RF pulse was output on each digitizer as a redundancy measure and to account for any delays between digitizers. The digitizer channels mapped to PMT numbers according to $5((board+1)\%+channel+1 = PMT$. Early in the neutron run, the digitizer ouput was increased from 1024 samples to 2048 samples. This change was made to capture a larger portion of the the slow ($\tau = 1.5$ μs) component of argon scintillation. Additionally, a larger pre-window insured that unknown cable and electronic delays in the accelerator RF pulse world not prohibit a time-of-flight measurement. Figure 6.11 shows an example beam event.

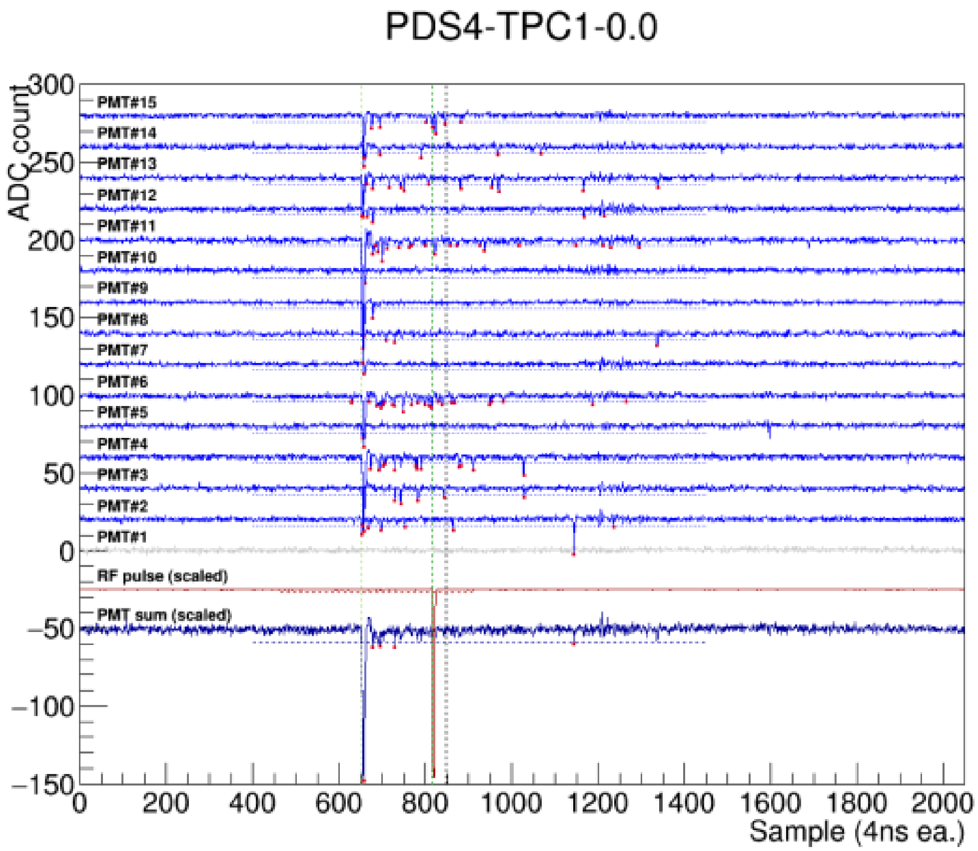

Figure 6.11: PDS event display showing an example beam event. Red points indicate event hits, vertical dashed lines indicate event time (prompt time and accelerator RF), and horizontal dashed lines indicate search windows and hit threshold. The accelerator RF pulse occurs after the prompt signal due to cabling and electronics delays.

The PDS data acquisition (DAQ) stores three timestamps per trigger: a GPS timestamp, a digitizer timestamp, and a computer timestamp. The GPS timestamp is synchronized with the TPC and enables synchronization between the PDS and TPC. The digitizer timestamp is local to each digitizer and can be used to correct for delays between digitizers. Soon after the neutron run, it was discovered that the digitizer timestamp was not read out. Additionally, due to the lack of a buffer on the GPS module, only the first timestamp in each TPC trigger was stored. The computer time was read out, but was unreliable due to large jitter. These difficulties have kept the TPC and PDS data from being synchronized and combined. In principle, the PDS time is the time of the interaction. The difference between the interaction time and readout time gives the drift time for each event which would allow reconstruction of the third spatial coordinate (z) for each track in the TPC. The inability to synchronize the PDS and TPC times is the reason this analysis is based solely on PDS data.

During the run, the PDS trigger threshold was set at a relatively low-level to trigger on as many events as possible. This has the side-effect of triggering the PDS on a large number of noise events, possibly related to the cryogenics pump. The 14 active PMTs performed well without individual gain adjustments. Single photoelectron (pe) pulses were clearly visible on all PMTs. The observed ringing of the PMT output after large pulses (see Figure 6.11) can be attributed to the PMT bases. This can be improved through individual impedance matching. Combined, the effects of the PMT ringing and the noisy trigger have proved difficult to separate signal from noise efficiently, as the noise events are above the photoelectron analysis threshold of 1/2 pe. However, examining the ratio of nearby hits and requiring more than 3 pe coincident in a PDS trigger removes many of these noise triggers.

A TPC-independent analysis was developed by the collaboration to examine the PDS data from the neutron run [59]. The calibration LEDs in the TPC were used to determine the single pe response of each PMT. These values were then used to discriminate hits using a 1/2 pe threshold. Hits are then grouped into an event, identifying the prompt light as the largest hit. To remove the effects of pile-up on subsequent analysis, any events with multiple prompt signals are flagged. A prompt time is interpolated and individual PMT hits are integrated to determine the total number of pe across time in the event.

6.2.1 Neutron Energy Spectrum from PDS data

The time of flight of a neutron is shown in Figure 6.12. The gamma peak is clearly seen around 70 ns. The peak is more narrow compared to the scintillator time of flight spectrum. Most likely gamma rays are blocked by the cryostat, so there are fewer gamma rays in the TPC than in the scintillator.

As with the scintillator data, we fitted the gamma peak with a Gaussian and subtracted the Gaussian from the distribution. The time of flight distribution after removing the gamma ray peak is shown in Figure 6.13.

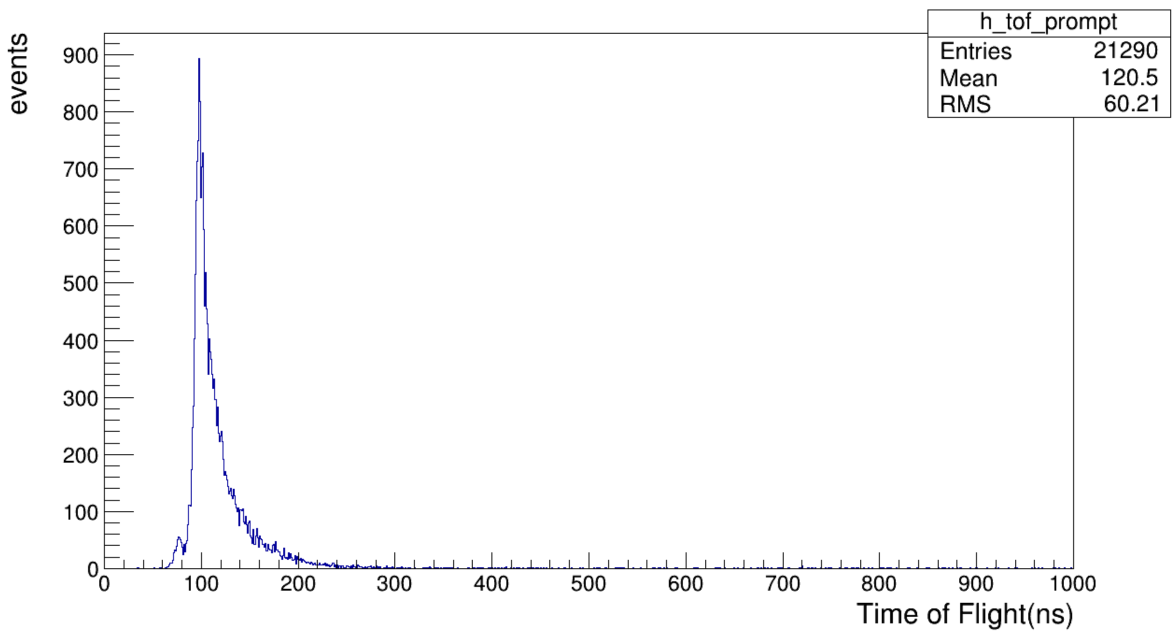

Figure 6.12: Time of flight distribution from PDS data. The peak near 70 ns is due to gamma rays.

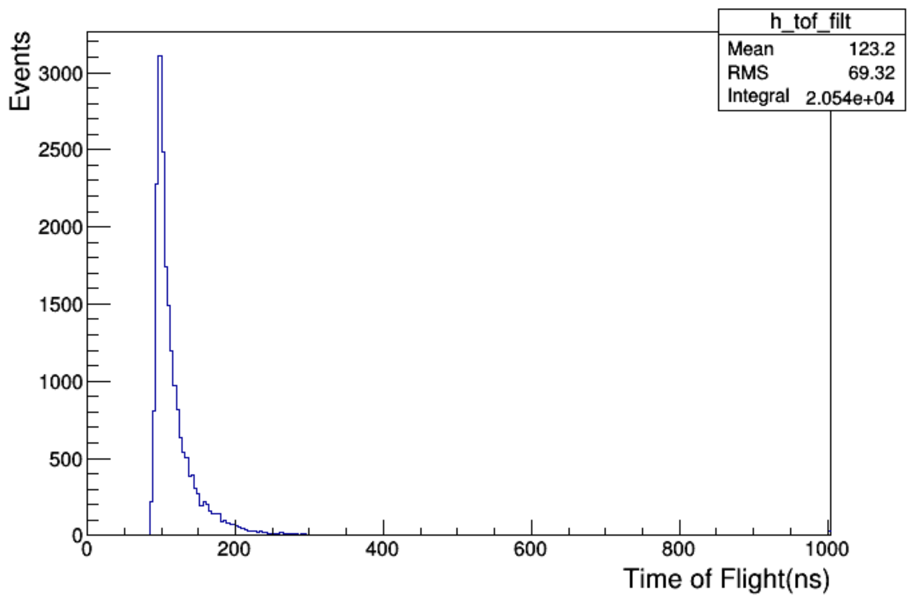

Figure 6.13: Time of flight of neutrons from their production point to mini-CAPTAIN using PDS data.

Figure 6.14 shows the neutron kinetic energy distribution based on the time of flight distribution shown in Figure 6.13.

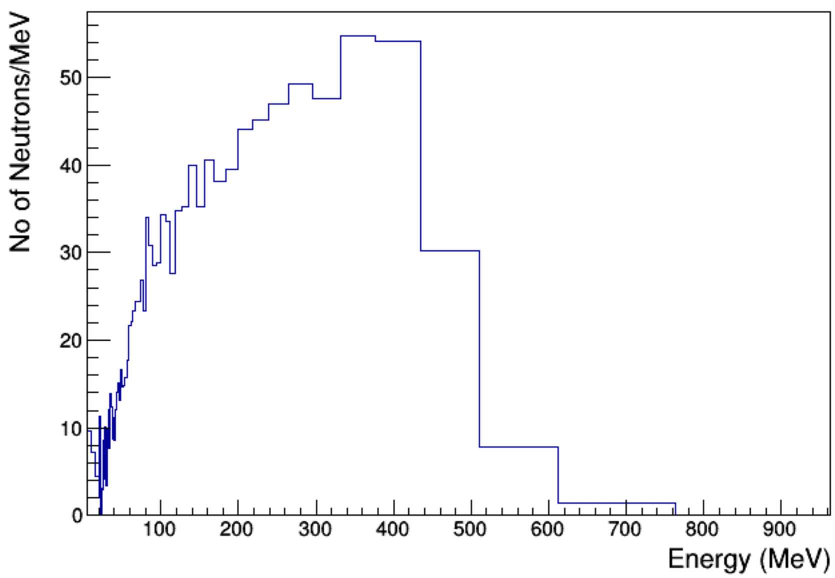

Figure 6.14: Normalized neutron energy from PDS data in MeV. The y-axis is number of neutrons per MeV. Each bin corresponds to 4 ns in time of flight.

6.2.2 Future Work

In future analyses, the neutron energy spectrum will be used to measure the neutron-argon cross section. The neutron flux will be determined from the scintillator data and simulation studies will be used to determine the efficiency of neutron detection in the mini-CAPTAIN PDS. Given the efficiencies, the neutron-argon cross section can be calculated. The cross section is given by

$$\sigma = \frac{R}{I\ N}, \tag{6.4}$$

where R is reaction per sec per volume and I is the number of interaction per sec per cm^2. N is number of argon atom per cm^3. N can be calculated by

$$N = \frac{\rho A}{M}, \tag{6.5}$$

where $\rho = 1.3954$ g/cm^3 density of argon, atomic mass $M = 39.948$ and A is Avogadro's number (6.023×10^{23}).

It is evident from the Figure 6.9 and 6.13 that there is not a one-to-one correspondence between neutrons detected by the scintillator and neutrons detected by the PDS. The overall ratio was $\approx$3. Figure 6.15 shows the ratio of neutron interactions in argon to those in scintillator as a function of neutron energy. The flux cancels in the ratio, so it is ratio of cross sections convoluted with detector efficiency. It is evident that the PDS has a low efficiency for detection of low-energy neutrons. However, overall the PDS sees more neutron interactions than the scintillator. So far simulation shows that neutrons interacting outside the TPC produces light that the PMTs inside the TPC can detect. Additionally, neutrons interacting in the cryostat can produce a cascade of particles, further complicating the situation. More study is needed to understand the efficiency and background contamination in the PDS analysis.

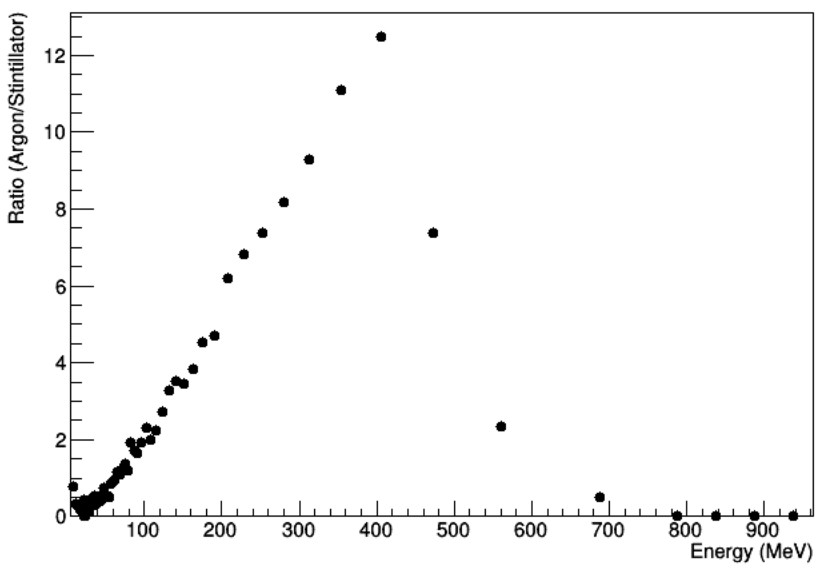

Figure 6.15: Ratio of number of measured neutron interactions in argon to those measured in the Scintillator.

6.2.3 Background

After the neutron run, background rate tests were performed to determine the contribution of cosmic rays, radioactive decay, and other sources of light to the PDS signal. Figure 6.16 shows one such run taken 22 days after the neutron run. These tests were performed by recording data with the mini-CAPTAIN PDS when the neutron beam was off. The background rate varies by PMT, some as low as 150 Hz and one as high as 8.5 KHz. The mean background rate observed is 600$\pm$60 Hz/PMT. A rate of about 600-700 Hz corresponds to approximately 1.5 cosmic rays/ms. In the analysis search window of 4 μs, that is equivalent to 0.3% chance that a beam event is actually a cosmic ray.

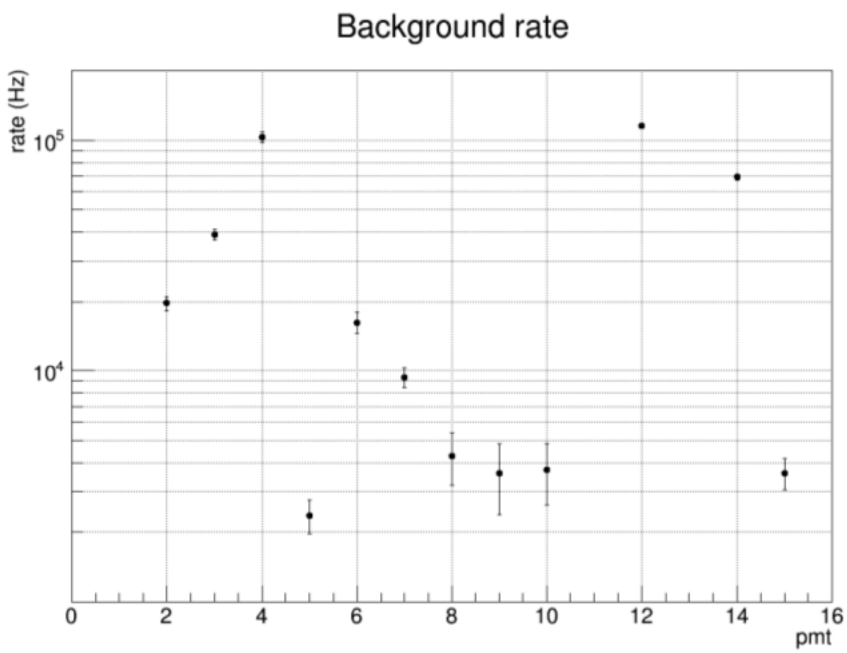

Figure 6.16: Background rate for individual PMT from one run of the mini-CAPTAIN PDS with no neutron beam.

6.3 Scintillation Yield

The measurement of the neutron time of flight presented in 6.2 allows us to study scintillation yield in argon as function of neutron kinetic energy. The relationship between time of flight and total photoelectrons (pe) from PMTs is shown in Figure 6.17.

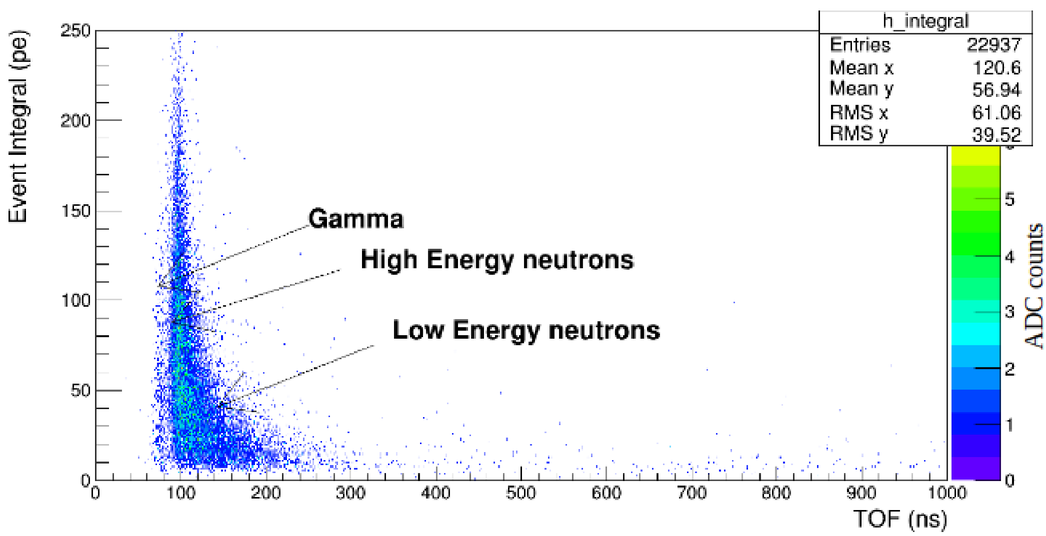

Figure 6.17: Event integrated PMT charge vs time of flight

Figure 6.18 shows the relation between triplet (slow component) and singlet (fast component) scintillation light. The singlet charge is the integrated charge of the first PMT hit, while triplet charge is computed as the integrated charge of all subsequent PMT hits. As explained in section 2.5, the ratio of the intensities of the two components depends on the ionization density and hence on the type of particle that ionizes the medium. Experimentally, we find a ratio of approximately 2 to 1 for the intensity of the triplet light to the singlet light in mini-CAPTAIN.

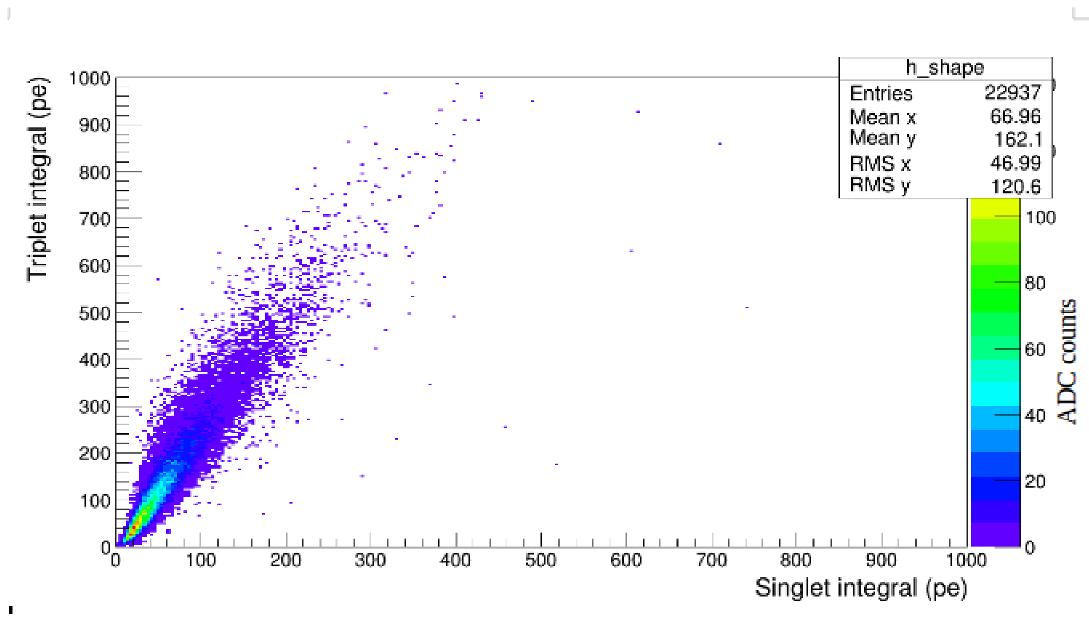

Figure 6.18: Relation between triplet light and singlet light

The scintillation yield is shown in Figure 6.19. This is the first measurement of relationship between the observed scintillation light as a function of neutron kinetic energy and photon yield in liquid argon. Understanding the scintillation yield from neutrons in liquid argon can help us to 1) separate background due to neutrons from the neutral current signature of supernova neutrinos and 2) better recover the missing energy of neutrons in beam neutrino interactions.

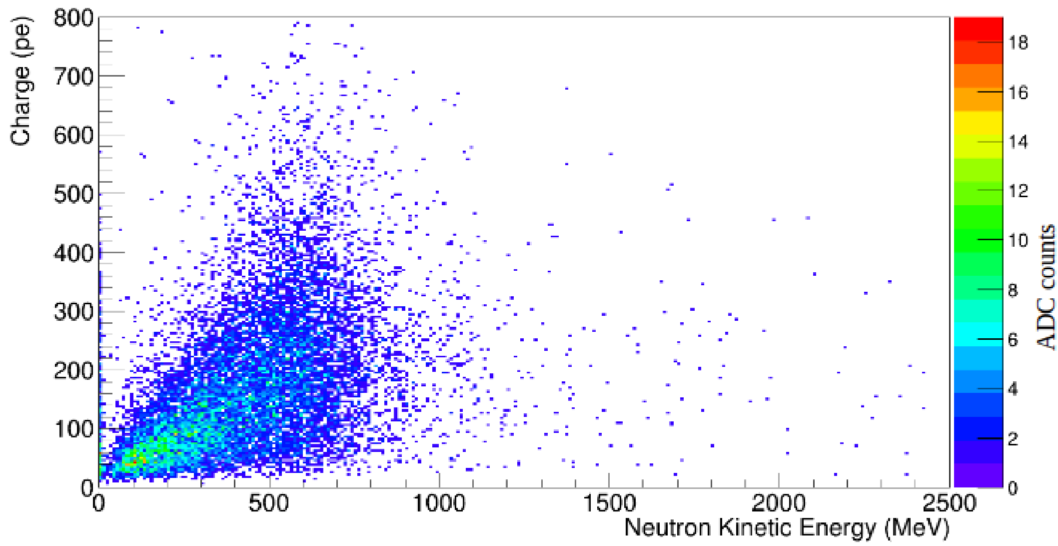

Figure 6.19: Total integrated charge detected by PMTs per event vs the neutron kinetic energy.

The Laundau convoluted most probable value is plotted in Figure 6.20 which shows the photon yield is linearly dependent on energy up to 500 MeV. From the extrapolation, light yield threshold is around 40 MeV. The plateau at about 500 MeV is probably due to the events not being contained.

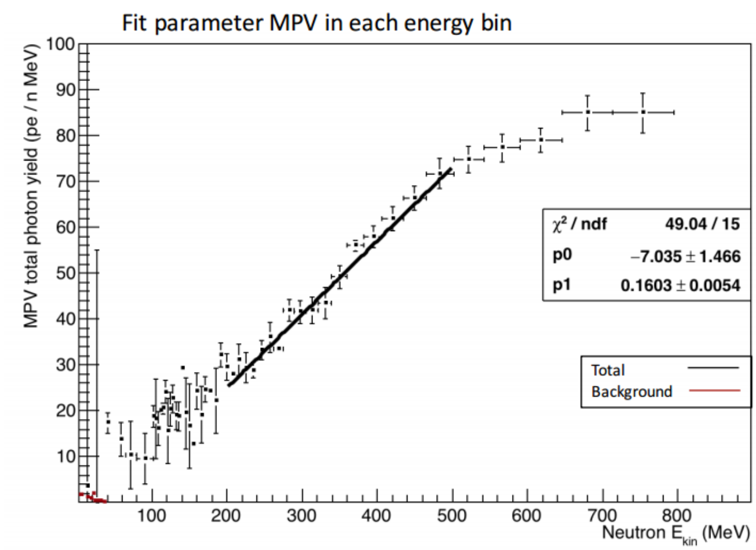

Figure 6.20: Laundau most probable value of photon yield as a function of neutron kinetic energy. Plot courtesy of P. Madigan [60].

Chapter 7

Conclusions

For the first time, we have studied neutron interactions in the energy range 20-800 MeV in a liquid argon TPC. I developed an algorithm to analyze the scintillator data, which will be used to determine the absolute neutron flux in future measurements, and discovered a source of background in the scintillator spectrum, possibly due to neutron reflection off the cryostat. I measured the neutron energy spectrum in mini-CAPTAIN based on data from the PDS using the time of flight technique. The spectrum was then used to find the scintillation yield in liquid argon as a function of neutron kinetic energy, which appears to be linear up to 500 MeV.

The mini-CAPTAIN detector is expected to take more neutron data in 2017. The same analysis described in this thesis will be applied to future data sets. With a measurement of the absolute neutron flux from the scintillator and a better understanding of the neutron detection efficiency of mini-CAPTAIN's PDS, the neutron-argon cross section can be measured. Furthermore, when the PDS and TPC data can be properly synchronized, the ionization signature of neutrons can be studied in addition to the scintillation signature. This and future data sets can be used to improve scintillation modeling in LArTPCs. These studies can be of great value to the DUNE experiment in developing algorithms to recover missing energy from neutrons in beam neutrino interactions and understanding the signal and background for supernova neutrino detection in the NC channel.

Bibliography

[1] S. Amerio et al. Design, construction and tests of the ICARUS T600 detector. *Nucl. Instrum. Meth. A*, 527:20–23, 2004.

[2] M. Apollonio et al. Limits on neutrino oscillations from the Chooz experiment. *Phys. Let. B*, 466:255–260, 1999.

[3] J. Beringer et al. Review of Particle Physics(Particle Data Group) . *Phys. Rev. D*, 86:121–125, 2012.

[4] R. Acciarri et al. `https://arxiv.org/pdf/1601.05823.pdf`, 2016. [Online; accessed 15-August-2016].

[5] C. Kraus et al. Final results from phase II of the Mainz neutrino mass search in tritium beta decay. *Eur. Phys. J.*, C 40:447–468, 2005.

[6] V. N. Aseev et al. Upper limit on the elctron antineutrino mass from the Troitsk experiment. *Phys. Rev. D*, 84:698–704, 2011.

[7] M. Osipowicz et al. A next generation tritium beta decay experiment with sub-eV sensitivity for the electron neutrino mass. *Phys. Rev. A*, 5:20–22, 2001.

[8] F. Hartmann and R. Naumann. Observation of N and M orbital-electron capture in the decay of Ho-163. *Phys. Rev. C*, 31:1594–1596, 1985.

[9] A. Nucciotti. Neutrino mass calorimetric searches in the MARE experiment. *Nucl. Phys. Proc. Suppl.*, 229-232:155–159, 2012.

[10] A. Himmel and K. Scholberg. Supernova Neutrino Detection. *Nucl. Part. Phys. Proc.*, 273-275:1897–1901, 2016.

[11] K. Hirata et al. Observation of a Neutrino Burst from the Supernova SN 1987a. *Phys. Rev. Lett.*, 58:1490–1493, 1987.

[12] R. M. Bionta et al. Observation of a Neutrino Burst in Coincidence with Supernova SN 1987a in the Large Magellanic Cloud. *Phys. Rev. Lett.*, 58:1494–1498, 1987.

[13] E. N. Alekseev et al. Possible Detection of a Neutrino Signal on 23 February 1987 at the Baksan Underground Scintillation Telescope of the Institute of Nuclear Research. *JETP Lett.*, 45:589–592, 1987.

[14] M. Aglietta et al. On the event observed in the Mont Blanc Underground Neutrino observatory during the occurrence of Supernova 1987a. *Europhys. Lett.*, 3:1315–1320, 1987.

[15] D. Schramm and J. Truran. New physics from Supernova SN1987A. *Phys. Rept.*, 189:89–126, 1990.

[16] G. Tammann et al. The Galactic supernova rate. *Astrophys. J. Suppl.*, 92:487–493, 1994.

[17] A. Mirizzi et.al. Earth matter effects in supernova neutrinos: Optimal detector locations. *JCAP*, 0605:12–15, 2006.

[18] G. G. Raffelt. Neutrinos and the stars. *Proc. Int. Sch. Phys. Fermi*, 182:61–143, 2012.

[19] `https://inspirehep.net/record/1253116/files/arXiv:1309.1740.pdf`, 2013. [Online; accessed 04-July-2015].

[20] C. Rubbia. The Liquid Argon Time Projection Chamber:A New Concept for Neutrino Detectors. *CERN-EP*, 77:01–08, 1977.

[21] C. Patrignani et al. Review of Particle Physics. *Chin. Phys. C*, 40(10):335–340, 2016.

[22] E. Aprile et al. *Noble Gas Detectors.* Wiley, 2008.

[23] L. Onsager. Initial Recombination of Ions. *Phys. Rev. B*, 54:554–557, 1938.

[24] U. Sowada et al. Hot-electron thermalization in solid and liquid argon,krypton and xenon. *Phys. Rev. B*, 25:244–248, 1982.

[25] C. Thorn. *Properies of LAr.* , volume 1. MicroBooNE Experiment, 2009.

[26] J. Thomas and D. A. Imel. Recombination of electron-ion pairs in liquid argon and liquid xenon. *Phys. Rev. A*, 36:614–616, 1987.

[27] R. Acciarri et al. A study of electron recombination using highly ionizing particles in the ArgoNeuT Liquid Argon TPC. *JINST*, 8:805–811, 2013.

[28] B. Baller et al. A Study of electron recombination using highly ionizing particles in the ArgoNeuT liquid argon TPC . *Journ. of Instrum.*, 8:220–222, 2013.

[29] J. B. Birks. *The Theory and Practice of Scintillation Counting*, volume 24. International series of Monographs on Electronics and Instrumentation, 1964.

[30] S. Amoruso et al. Study of electron recombination in liquid argon with the ICARUS TPC. *Nucl. Instrum. Meth. A*, 523:275–286, 2004.

[31] A. Hitachi. Exciton kinetics in condensed rare gases . *J. Chem. Phys.*, 80:478–480, 1984.

[32] M. A. Hofmann. *Liquid Scintillators and Liquefied Rare Gases for Particle Detectors*. PhD thesis, Technische Univesity at Munchen, 2012.

[33] S. Kubota et al. Recombination luminescence in liquid argon and in liquid xenon. *Phys. Rev. B*, 17(6):2762–2765, 1978.

[34] J. Splitz et al. A regenenrable filter for liquid argon purification . *Nucl. Instum. A*, 605:2009, 306-311.

[35] E. Aprile et al. *Noble Gas Detectors*. Wiley, 2008.

[36] F. Bloch and N. Bradbury. On the Mechanism of Unimolecular Electron Capture. *Phys. Rev. B*, 48:689–695, 1935.

[37] A. Herzenberg. Attachment of slow Electrons to Oxygen Molecules . *J. Chem. Phys.*, 51:11–15, 1969.

[38] O. Bunemann et al. Design of grid ionization chambers . *Can. J. of Research*, 27:191–206, 1949.

[39] M. Schenk. Studies with a liquid argon time projection chamber : addressing technological challenges of large-scale detectors. Master's thesis, Bern University, Wiesbaden, 2014.

[40] V. Radeka et al. Cold electronics for 'Giant' Liquid Argon Time Projection Chambers. *J. Phys. Conf. Ser.*, 308:12–21, 2011.

[41] S. Amerio et al. Design, construction and tests of the ICARUS T600 detector. *Nucl. Instrum. Meth. A*, 527:329–410, 2004.

[42] C. Anderson et al. The ArgoNeuT Detector in the NuMI Low-Energy beam line at Fermilab. *JINST*, 7:100–105, 2012.

[43] B. Fleming. *The MicroBooNE Technical Design Report* , volume 3. MicroBooNE, 2012.

[44] N. Saitseva et al. Scintillation properties of solution-grown trans-stilben single crystal. *Nucl. Instrum. Meth. A*, 789:08–15, 2015.

[45] R. Bowles. Analysis of scintillation pulse shapes for stilbene using neutron and gamma-ray excitation. *Nucl. Instr. Meth. A*, 192:200–204, 1961.

[46] `http://www.hamamatsu.com/us/en/index.html`, 2015. [Online; accessed 04-July-2016].

[47] M. Suzuki et al. Time dependence of the recombination luminescence from high-pressure Argon, Krypton and Xenon excited by alpha particles . *Nucl. Instr. Meth. A*, 192:565–574, 1982.

[48] R. S. Mulliken. Potential curves of diatomic raregas molecules and their ions, with particular reference to Xe2 . *J. Chem. Phys.*, 52:24–23, 1970.

[49] M. Tanaka et al. LET dependence of scintillation yields in liquid xenon. *Nucl. Instrum. Meth. A*, 457:454–463, 2001.

[50] S. Himi et al. Liquid and solid argon, and nitrogen doped liquid and solid Argon Scintillators. *Nucl. Instrum. Meth. A*, 203:153–157, 1982.

[51] R. Acciarri et al. Effects of Nitrogen and Oxygen contamination in liquid Argon. *Nucl. Phys. Proc. Suppl.*, 197:70–73, 2009.

[52] V. M. Gehman et al. Fluoresescence Efficiency and Visible Re-emission Spectrum of Tetraphenyl Butadiene Films at Extreme Ultraviolet Wavelengths . *Nucl. Instr. Meth. A*, 654:25–32, 2011.

[53] D. Gastler. *Design of single phase liquid argon detectors for dark matter searches*. PhD thesis, Boston University, 2012.

[54] D. Gastler et al. Measurement of scintillation efficiency for nuclear recoils in liquid argon. *Phys. Rev. C*, 85:650–653, 2012.

[55] R. Acciarri et al. Neutron to gamma pulse shape discrimination in liquid argon detectors with high quantum efficency photomultiplier tubes . *Phys. Pro.*, 37:250–254, 2012.

[56] https://geant4.web.cern.ch/geant4/, 2016. [Online; accessed 04-July-2015].

[57] http://rat.readthedocs.io/en/latest/overview.html, 2016. [Online; accessed 20-July-2016].

[58] P. W. Lisowski et al. The Los Alamos Neutron Science Center . *Nucl. Instrum. Meth. A*, 562:910–914, 2006.

[59] P. Madigan. http://nngroup.physics.sunysb.edu/~captain/DocDB/0006/000605/001/PDSAnalysisOverview.pptx.pdf, 2016. [Online; accessed 15-August-2016].

[60] P. Madigan. http://nngroup.physics.sunysb.edu/~captain/DocDB/0006/000619/001/PDSAnalysisUpdate-NeutronData.pdf, 2016. [Online; accessed 15-August-2016].